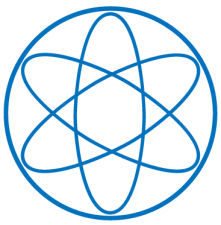

Strange Multibaryon Systems: Predictions and Experiments

Masterarbeit von Ana Solaguren-Beascoa Negre

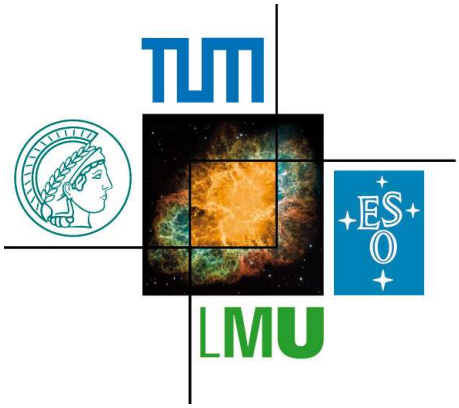

Physik Department - Technische Universität München

Excellence Cluster - 'Origin of the Universe'

I would like to start my work thanking all the people who have helped me during the project, and have made it possible. In first place, Laura Fabbietti, not only for the academical opportunity she has given to me, but also for the personal support during my whole stay in Munich. Obviously, Eliane Epple, for her pacience during the whole project and the long hours she has invested introducing me to the world of experimental particle physics, teaching me how to work in science and making me learn german as soon as I arrived in Munich. Also to all the people working in the group, mainly the ones working in the same room as me (even if they always ate my cookies). It was a pleasure to work with all of you.

Àngels Ramos, perque gràcies a ella he pogut col·laborar en aquest projecte, treballar en aquest grup i començar a entendre el món de la física de partícules.

Finally, my family and friends who have been supporting me during my whole stay in Munich and have been trying to understand what a kaonic bound state is and how to look for it. Gràcies.

Abstract

In the last few years some publications have shown that the strong interaction between a K^- and a proton lead to the assumption of the ppK^- bound state existence. Experimental results, such as the FINUDA [12] or DISTO collaboration [22], showed a signal for the invariant mass of $p\Lambda$ which could be identified with a ppK^- bound state.

This thesis shows the HADES experimental data for a p+p collision at 3.5 GeV, studying events which contain a final $pK^+\Lambda$ state in order to analyze the existence of the ppK^-. A first exhaustive study was done by simulating the ppK^- together background channels which could contribute to the final experimental signal. An analysis using the experimental data was carried out following the DISTO collaboration study using a direct $pK^+\Lambda$ production using the COSY-TOF collaboration results for the Λ angular distribution. This first analysis did not describe the experimental data correctly, therefore, a further study of the data was done, including four different N*-resonance masses together with the direct $pK^+\Lambda$ production in the simulation. This second study could reproduce quite well most of the experimental data except for some observables such as the invariant mass for the $p\Lambda$.

Contents

Chapter 1

Introduction

The possible existence of a ppK^- bound state has been studied in this work through the analysis of the HADES experimental data. This kaonic cluster was theoretically predicted after assigning a strong binding energy to the interaction between a K^- and a proton as a strong $\bar{K}N$ attraction. The strong force produced by the K^- on the proton should produce a K^-p deep bound state. In 2006 it was predicted that the $\Lambda(1405)$, understood as a double pole resonance coupled to a K^--proton quasi bound state and a $\pi\Sigma$ molecule, could originate a ppK^- bound state when produced together with a proton [25]. The understanding of the $\Lambda(1405)$ signal is therefore important to extract the strength of the K^-p interaction and thus, check on the possible existence of a ppK^- bound state.

1.1 The $\Lambda(1405)$

The $\Lambda(1405)$ appears in the PDG as a known resonance with the following properties [10]:

Spin	Isospin	Strangeness	J^P	Mass	Width
1/2	0	-1	$\frac{1}{2}^-$	1406.5 MeV/c^2	50 MeV/c^2

Table 1.1: Properties of the $\Lambda(1405)$

It was first observed by the ALSTON 61B experiment [13] in a $K^-p \rightarrow \Sigma\pi\pi\pi$ reaction at 1.15 GeV/c. As its mass is found to be 30 MeV/c^2 below the $\bar{K}N$ threshold, it could only be observed through a direct $\pi\Sigma$ decay. The $\Lambda(1405)$ could not be explained through the quark model picture as an excited state of an up-down-strange quark system. Thus, R. H. Dalitz speculated that the $\Lambda(1405)$ might not be an excited state of 3-quarks but emerges dynamically from the composition of a K^--proton quasi bound state and a $\pi\Sigma$ molecule. The fact that the

Λ(1405) lies close below the $\bar{K}N$ threshold prevents the usage of chiral perturbation theory to model the interactions that lead to the formation of resonance. Instead, effective field theory is used to describe this state[15]. The meson-baryon interaction has been built by theory exploiting a meson-baryon chiral effective Lagrangian $\mathcal{L}_{eff}(B,U)$, to work with hadronic degrees of freedom only, but preserving the essential symmetries of the QCD Lagrangian, which describes the strong interaction of quarks and gluons as degrees of freedom:

$$\mathcal{L}_{eff}(B,U) = \sum \mathcal{L}_{2n}^{M}(U) + \mathcal{L}_{n}^{MB}(U,B) \tag{1.1.1}$$

where $\mathcal{L}_{2n}^{M}(U)$ corresponds to the meson Lagrangian at order 2n in perturbation theory, which contains the octet of Nambu-Goldstone bosons (K, η, π) , collected as a matrix form in Φ (or in the U chiral field) and $\mathcal{L}_{n}^{MB}(U,B)$ corresponds to the Lagrangian of the meson-baryon interaction to order n in chiral perturbation theory, which contains the baryon octet field (N,Λ,Σ,Ξ) in the B matrix.

$$\Phi = \begin{pmatrix} \frac{1}{\sqrt{2}}\pi^0 + \frac{1}{\sqrt{6}}\eta & \pi^+ & K^+ \\ \pi^- & -\frac{1}{\sqrt{2}}\pi^0 + \frac{1}{\sqrt{6}}\eta & K^0 \\ K^- & \overline{K}^0 & \frac{-2}{\sqrt{6}}\eta \end{pmatrix}$$

$$B = \begin{pmatrix} \frac{1}{\sqrt{2}}\Sigma^0 + \frac{1}{\sqrt{6}}\Lambda & \Sigma^+ & p \\ \Sigma^- & -\frac{1}{\sqrt{2}}\Sigma^0 + \frac{1}{\sqrt{6}}\Lambda & n \\ \Xi^- & \Xi^0 & \frac{-2}{\sqrt{6}}\Lambda \end{pmatrix}$$

$$U = e^{i\frac{\sqrt{2}\Phi}{f}}$$

The meson-baryon scattering amplitude at lowest order, also known as Weinberg-Tomozawa interaction, corresponds to:

$$V_{ij}^{WT}(W) = -\frac{C_{ij}}{4f^2}(2W - M_i - M_j)\sqrt{\frac{M_i + E_i}{2M_i}}\sqrt{\frac{M_j + E_j}{2M_j}} \tag{1.1.2}$$

where W is the total energy of the process at the center of mass frame, C_{ij} are SU(3) Clebsch-Gordan coefficients which contain the sign and strength of the interaction depending on the meson-baryon channel. V_{ij} is regarded as the potential of the scattering equation for the Chiral Unitary Model.

Resonances must be calculated using the whole perturbation series for the T matrix, calculated from the Lippmann-Schwinger equation for a quantum state

$$|\psi\rangle = \left|\overrightarrow{k}\right\rangle + GV\left|\overrightarrow{k}\right\rangle + GVGV\left|\overrightarrow{k}\right\rangle + ... \tag{1.1.3}$$

where $|\psi\rangle$ stands for the scattered wave function, $\left|\overrightarrow{k}\right\rangle$ are the eigenstates of the free Hamiltonian, G is the Green function for the Schrödinger equation and V the potential of the system. After

applying V on both sides to the expression of the wave function , one obtains the Bethe-Salpeter equation 1.1.4:

$$T = V + VGV + VGVGV + ... = V + V \cdot G \cdot T \tag{1.1.4}$$

which is represented in fig. 1.1. V then corresponds to the interaction kernel and G corresponds to the meson-baryon loop function.

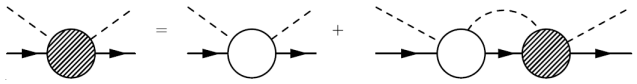

Figure 1.1: Schematic illustration of the T matrix (shaded blob) as an expansion of V terms (empty blobs). Dashed lines represent mesons, solid lines represent baryons.

At an energy close to a resonance, the T-matrix can be written as a sum of a Breit-Wigner function and background contribution (where W is the CM energy):

$$T_{ij}(W) = \frac{g_i g_j}{W - M_R + i\frac{\Gamma_R}{2}} + T_{ij}^{BG} \tag{1.1.5}$$

which has a pole at

$$z_R = M_R - i\frac{\Gamma}{2} \tag{1.1.6}$$

The unitary chiral perturbation approach explained the $\Lambda(1405)$ resonance as a double-pole. The high energy pole coupled to the $\bar{K}N$ channel and the low energy to the $\pi\Sigma$ one. Figure 1.2 shows the $\Lambda(1405)$ poles represented on the complex plane. In the physical real axis, the contribution of each one of the poles may vary depending on the characteristics of the experimental reaction. This has been proved, as different experiments show a different shape for the $\Lambda(1405)$ mass. Figure 1.3 shows the invariant mass ($\mathrm{IM}_{\pi\Sigma}$) from a $K^- p$ reaction at 4.2 GeV/c for the data (bars) described by the $\pi\Sigma \to \pi\Sigma$ and $\bar{K}N \to \pi\Sigma$ amplitudes, which can be explained as a superposition of $\bar{K}N$ and $\pi\Sigma$ pole contributions. The contribution of the two poles to the formation of the $\Lambda(1405)$ is of crucial importance for the interpretation of the resonance, which, if mainly consituted by a $\bar{K}N$ state, might imply the existence of a ppK^- bound state.

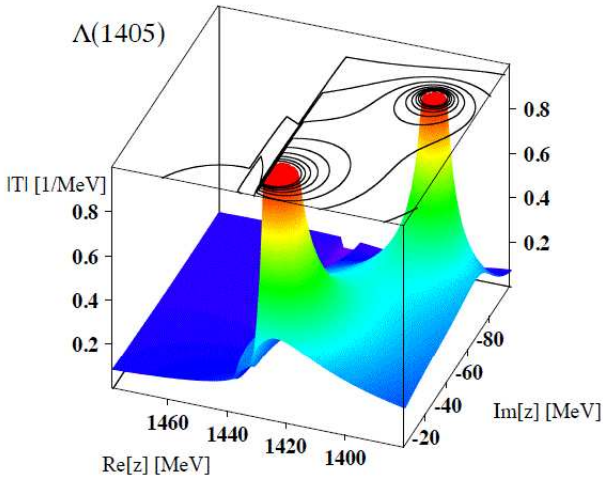

Figure 1.2: Absolute value of the T matrix, divided in real an imaginary part for the Λ(1405).

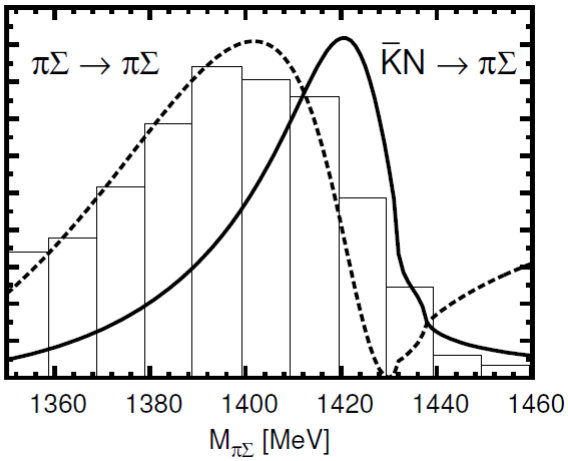

Figure 1.3: $IM_{\pi\Sigma}$ taken from [20]. Dashed lines correspond to the $\pi\Sigma \longrightarrow \pi\Sigma$ amplitude, continuous line corresponds to $\bar{K}N \longrightarrow \pi\Sigma$ one. The histogram corresponds to experimental data [16].

1.2 Experimental search for Kaonic bound states

The Λ(1405) was also described as a unique K^-p bound state, with a binding energy of 27 MeV [21]. This theoretical interpretation was exploited to speculate on the possible existence of a ppK^- bound system and a three-body calculation predicted a binding energy of 48 MeV. These

results were criticized on [19], where the $\pi\Sigma$ channel was included, using SU(3) chiral dynamics, together with the weak bound state $\bar{K}N$ and assigning a binding energy of 12 MeV to the latter.

Experimental results were published by the FINUDA collaboration [12] where they claimed to have found a ppK^- signal at around 2256 MeV/c^2 in the following reaction for stopped kaons:

$$K^-(^AZ) \rightarrow {}^{A-2}(Z-2)\ \Lambda\, p.$$

In this experiment the following nuclear targets were used: ^6Li, ^7Li, ^{12}C, ^{27}Al, ^{51}V. Figure 1.4 shows the measured Λp invariant mass. The analysis was done after selecting events with the Λ and the proton flying in opposite directions in the lab reference frame ($\cos\theta^{Lab}_{p\Lambda}$< -0.8) as shown in fig. 1.6 right, with a dashed region. This cut was applied, in order to select events in which the Λp pairs fly back to back in the ppK^- rest frame. The interpretation of this signal as a kaonic bound state was questioned in [26], where it was concluded that the peak could be explained by the scattering of the outcoming particles with the daughter nucleus. A theoretical simulation was done without including any ppK^- bound state in order to show that the experimental peak could be explained without it.

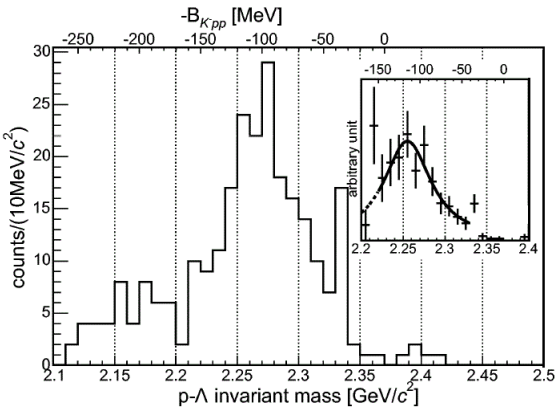

Figure 1.4: FINUDA data [12] showing the Λp invariant mass distribution with a peak at 2256 MeV/c^2.

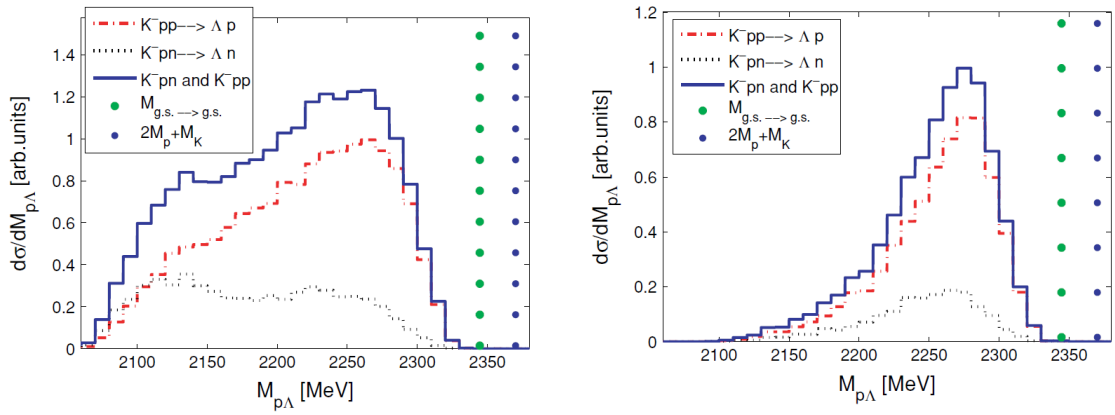

Figure 1.5: Theoretical representation [26] of FINUDA experimental data [12] using no ppK^- bound state. Left: $IM_{p\Lambda}$ with no angular selection. Right: $IM_{p\Lambda}$ with angular correlation selection ($\cos\theta^{Lab}_{p\Lambda}$< -0.8).

Figure 1.5 shows the theoretical prediction for the Λp invariant mass shown in fig. 1.4 [26], without (left) and with (right) angular selection ($\cos\theta^{Lab}_{p\Lambda}$< -0.8). The theoretical simulation considered the experimental back-to-back correlation for the emitted proton and the Λ. As the theoretical distribution of the opening angle between the proton and the Λ (fig. 1.6 left) did not exactly reproduce the experimental results (fig.1.6 right), thesis supported by the theoretical calculations is still under discussion [26].

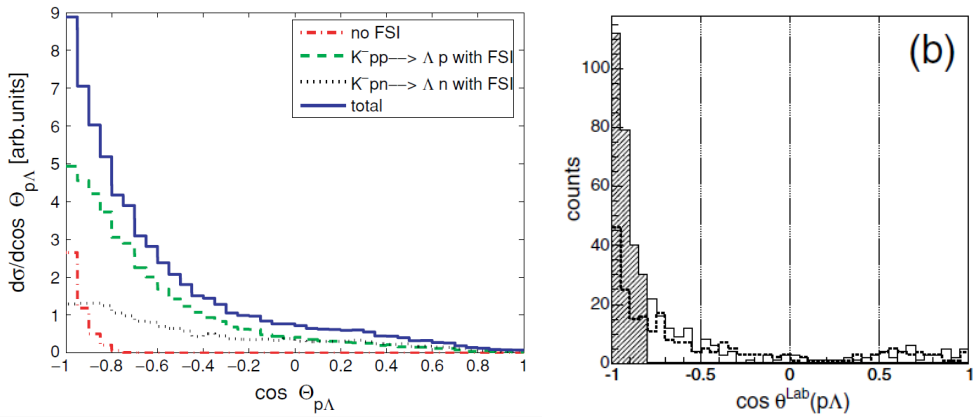

Figure 1.6: Left: Theoretical prediction for of the opening angle for the outcoming proton and Λ for the FINUDA experiment [26]. Right: Opening angle for the proton and Λ from FINUDA experimental data [12].

The DISTO collaboration also reported experimental data of a p+p at a beam energy of 2.85 GeV reaction [22]:

$$p + p \longrightarrow ppK^- + K^+$$

The ppK^- decay product was Λp. The missing mass K^+ (MM_{K^+})full-scale simulations including only the $pK^+\Lambda$ final state emitted according to the phase space.. The deviation spectra showed a peak at 2265 MeV/c^2 with an associated width and binding energy of 67 MeV and 115 MeV respectively. These values do not agree with the result published by FINUDA and discussed above.

Since the same reaction at the kinetic energy of 3.5 GeV has been measured with the HADES spectrometer, a similar analysis has been carried out within this master thesis to cross-chek the DISTO results. The study of the DISTO data lead to the conclusion that the large-angle cut (LAP) for the proton produced through the ppK^- decay ($0.6>|cos\theta_{CM,p}|$) enhanced the events containing the ppK^- production. A further cut on the Kaon polar angle was applied, as $-0.2<\cos\theta^{CM}_{K^+}<0.4$ selection seemed to select events produced in a two-body decay. These observables and the respective cuts are shown on fig. 1.7. Figure 1.8 shows the deviation spectrum for the MM_{K^+} after applying the cuts just mentioned [22]. It shows the data fitted with a Gauss function.

This work, in line with the previous experimental results, aims to add additional information to the ongoing kaonic bound state quest.

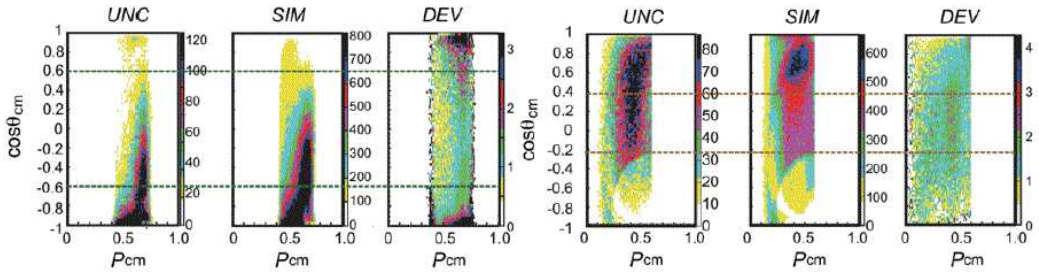

Figure 1.7: Momentum vs. cosθ at the CMS for uncorrected experimental (UNC), Simulated (SIM) and deviation (DEV) spectrum for (left) proton and (right) kaon published on [22]. The dashed lines show the cuts applied on fig. 1.8.

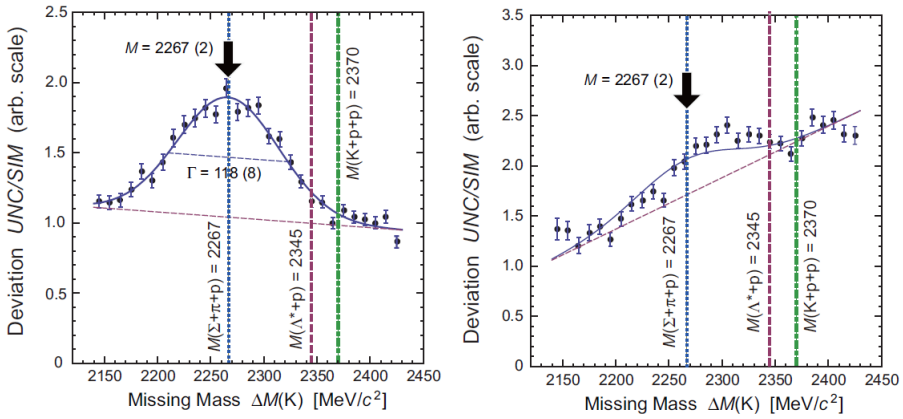

Figure 1.8: DISTO MM_{K^+} deviation spectra from experimental data [22] for (left) LAP ($0.6>|cos\theta_{CM,p}|$), and (right) SAP ($0.6<|cos\theta_{CM,p}|$).

Chapter 2

The HADES Detector

2.1 Experimental setup

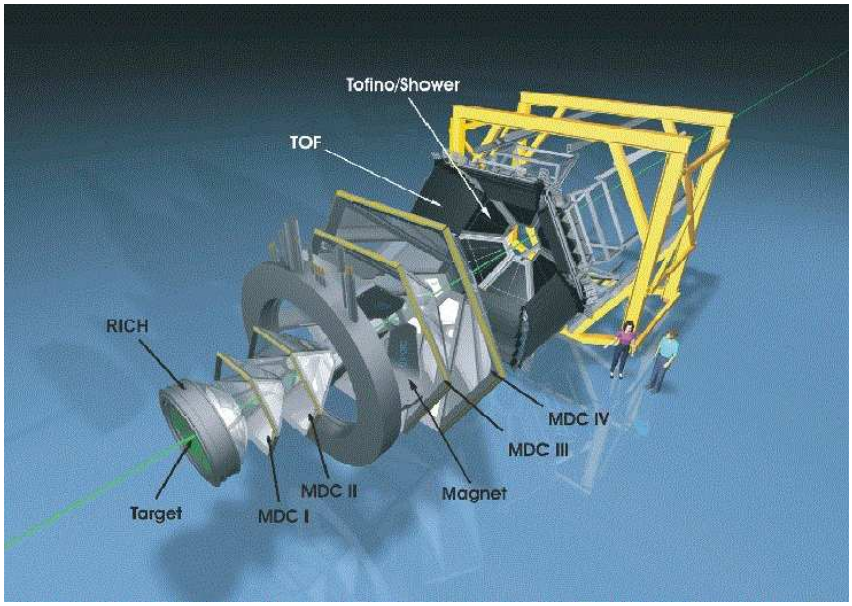

Figure 2.1: A scheme of the HADES spectrometer. The green line represents the beam direction

The High Acceptance Di- Electron Spectrometer (HADES) is located at the heavy-ion synchrotron (SIS) located at the Gesellschaft für Schwerionenforschung (GSI) in Darmstadt, Germany where fixed-target experiments with light and heavy nuclei as beams accelarated to kinetic energies between 1 and 4 GeV are carried out.

The main goal of HADES isto determine the form factors of vector mesons and baryons decaying into e^+e^--pairs and examine how the hadron properties change in hot and dense nuclear matter [14]. Light vector mesons decaying electromagnetically are very rare. In order to measure a high statistic of such events, the HADES detector covers 85% azimuthal acceptance [2] and polar angles from 18^o to 85^o (which corresponds only 45% of the solid angle, but still 50% of the dilepton decays will be emitted in this region).

The spectrometer is divided in different parts explained in the following paragraphs. Figure 2.2 shows an exploded side view of the detector.

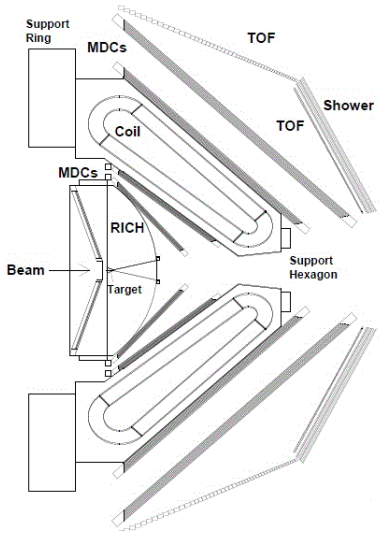

Figure 2.2: Side view representation of the HADES spectrometer.

2.1.1 The Reaction System

The experiment studied within this work is a proton-proton collision at a beam kinetic energy of E_{Kin}(p)=3.5 GeV. The proton beam was incident on a 5 cm long LH_2 target which was cooled to 20 K at an atmospheric pressure. A first level trigger was employed requiring at least 3 charged particles in the HADES acceptance for each event. A total number of $1.2{\cdot}10^9$ events were collected.

2.1.2 The RICH-Detector

The Ring Imaging Cherenkov detector (RICH) is designed to identify the e^+e^- pairs from rare vector meson decays. Figure 2.3 shows a schematic representation of the RICH detector with its two separated chambers. Cherenkov radiation starts when the velocity of a particle fullfills the relation $\beta > n^{-1}$, where n is the refraction index of the medium where the particle is travelling. This corresponds to a threshold gamma factor:

$$\gamma_{th} = \frac{1}{\sqrt{1 - \frac{1}{n^2}}}. \tag{2.1.1}$$

A particle with a gamma factor below γ_{th} does not induce a Cherenkov light cone. The Cherenkov radiation is then reflected by a spherical mirror and travels through a CaF_2 crystal which separates the radiator gas from the detector gas. The photons hit the CsI photocathodes which emit electrons. The anode wires will amplify the electron signal. This signal on the pads is interpreted by a pattern recognition software which finds rings. The RICH detector is thus able to detect different Cherenkov rings. From the radius of the rings, the different particles can be distinguished, as the opening angle follows eq. (2.1.2).

$$\theta_c = cos^{-1}\frac{1}{n\beta} \tag{2.1.2}$$

As electrons and positrons (0.511 MeV/c^2) are much lighter than hadrons (mass > 140 MeV/c^2), their gamma value is much higher than for the latter.

The threshold gamma value for the radiator gas (C_4F_{10}) is γ_{th}=18.3, that translates to a momentum threshold of few MeV/c for electrons and positrons and 2 GeV/c for pions. This way the RICH detector is hadron-blind.

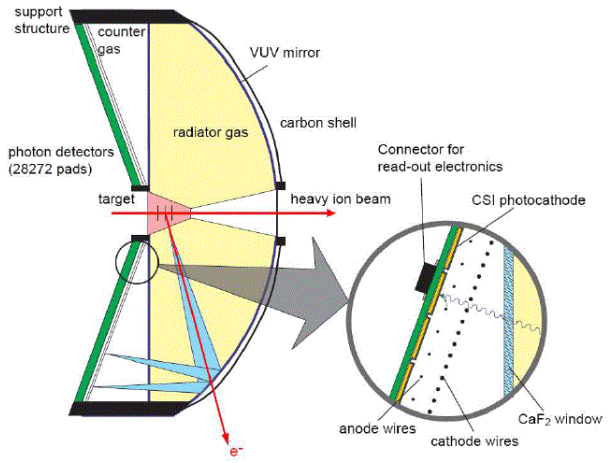

Figure 2.3: Side view of the RICH detector. The blue cone represents the Cherenkov radiation.

2.1.3 The Magnet

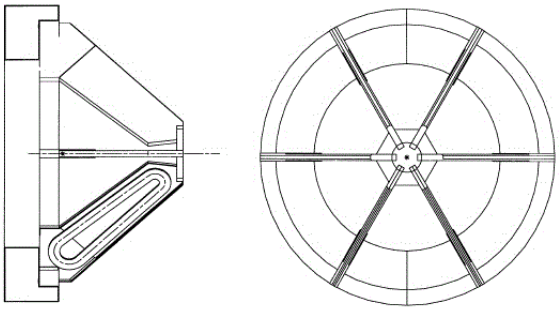

Figure 2.4: Vertical (*right*) and front view (*left*) of the magnet.

The superconducting toroidal magnet consist of 6 coils around the beam axis. The coils are separated from each other by an individual vacuum chamber. The magnet is represented in fig. 2.4. The field of 0.6 T produced by the magnet will deflect the charged particle's trajectory and will allow us to calculate the particle's momentum.

2.1.4 The MDC-Detectors

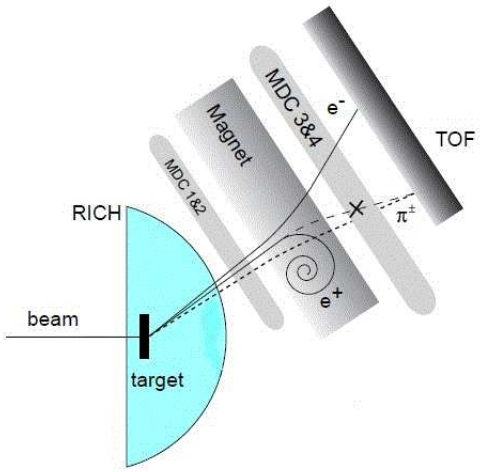

Figure 2.5: Representation of the Multiwire Drift Chambers (MDC)

The Multiwire Drift Chambers (MDC) are used to measure particle tracks and determine, together with the magnet momenta of particles . There are four modules, two behind and two

in front of the magnet (MDC III, MDC VI and MDC I, MDC II, respectively). Each module consists of six planes of wires which are orientated with different angles in order to get a higher space resolution of the hit points. If a charged particle passes a drift cell, it ionizes the counting gas (Helium and isobutane) [6], the electron clouds drift torwards the wire and the signal is picked up by a fast amplifier connected to the wire and transformed into an electronic signal. The MDC detectors are represented in fig. 2.5. The momentum of the particles is determined by the particle's path curvature inside the magnetic field.

2.1.5 The Time-of-Flight Detectors

The time-of flight detectors (TOF) are divided into two parts. The TOF detector is covering the polar angles from 44 to 88 degrees with 8 modules and the TOFino detector (inner TOF) covers from 15 to 44 degrees with 6 modules. Figure 2.6 shows a schematic representation of the TOF and the TOfino. They are used for particle identification, explained in more detail later. Plastic scintillators orientated perpendicularly to the beam axis placed in each of the modules, produce light when a charged particle traverses them. This light is detected by photomultiplier tubes. With the measured arrival signal and using the start signal, the time of flight of the particle can be then determined. The time resolution achieved with the TOF system is about 180 ps and for the TOFino about 300 ps. The height of the signal produced by the photomultipliers will allow us to calculate the energy loss dE/dx.

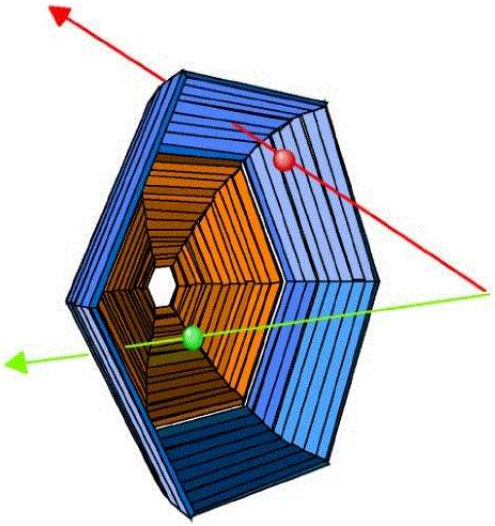

Figure 2.6: TOF (blue) and TOFino (orange) detectors. The scintillator strips are visible for both (black lines).

2.1.6 The PreShower

Behind the TOFino detector, a Pre-Shower detector has been placed for additional electron and positron identification in the forward direction. It consists of three wire chambers filled with isobutane-gas [2]. As particles fly through the detector, high energy photons are produced due to bremsstrahlung, creating with high probability an electron-positron pair which themselves might again produce new electron-positron pairs through bremsstrahlung. This leads to a high production of charged particles. The signal detected at the wire chambers will give the energy loss of the incident particle. This will be used to distinguish the different particles in the experiment (see 2.2.1).

2.1.7 The Forward Wall

The Forward Wall scintillator hodoscope was added during the proton-proton beam time at 3.5 GeV located 7.3 meters behind the RICH detector. It consists of [9] 140 small cells (4x4 cm^2), 64 middle cells (8x8 cm^2) and 84 big cells (16x16 cm^2). The Forward Wall measures the hit position, the time-of-flight with a precision of around 700 ps and the energy loss of an incoming charged particle.

2.2 Particle Identification

2.2.1 Energy loss reconstruction

A charged particle crossing a medium suffers energy loss through ionization. This energy loss per travelled distance is given by the Bethe-Bloch equation [14]:

$$-\frac{dE}{dx} = \frac{4\pi}{m_e c^2} \cdot \frac{nz^2}{\beta^2} \cdot \left(\frac{e^2}{4\pi\epsilon_0}\right)^2 \cdot \left[ln\left(\frac{2m_e c^2\beta^2}{I \cdot (1-\beta^2)}\right) - \beta^2\right] \tag{2.2.1}$$

where $\beta = v/c$, $z \cdot e$ is the particle charge, n the electron density of the target, I the mean excitation potential of the medium.

As the energy loss just depends on the charge of the particle and its velocity , the dE/dx represented as a function of momentum p (which depends on the mass of the particle), will be different for each particle's mass. An example of the dE/dx as a function of the momentum times the polarity of the particles is shown in fig. 2.7.

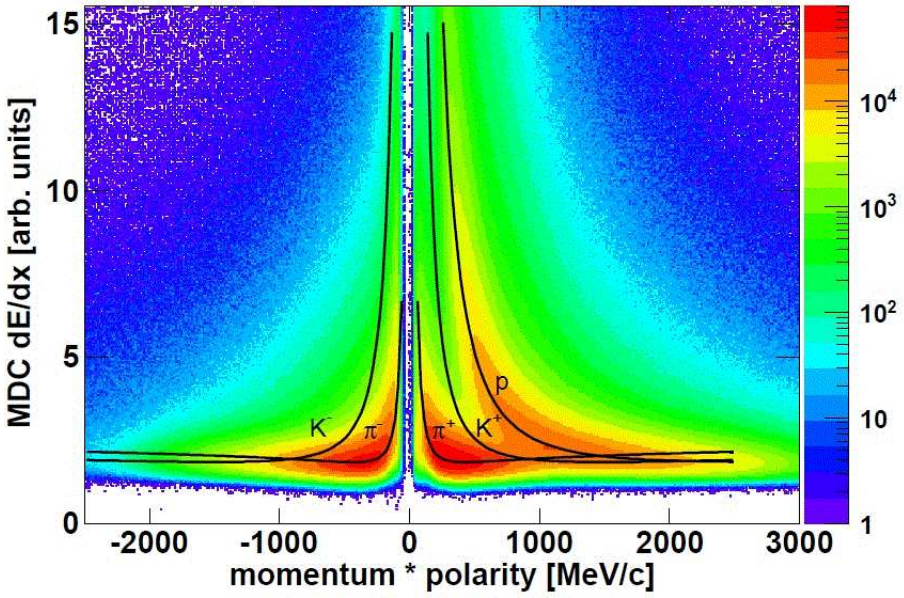

Figure 2.7: Particles energy loss as a function of momentum. Curves show regions where protons, pions and kaons are expected[8].

2.2.2 Time of Flight reconstruction

With the Time of Flight (TOF) detector the velocity of the particles can be measured, as the path length and the polarity of each particle can be reconstructed with help of the tracking inside the magnetic field. After crossing the magnetic field, each particle has a bending of its trajectory according to its mass and charge. The momentum can be determined from the bending of the particle's trajectory. From eq. (2.2.2) the mass of each particle can be calculated due to this mass, the particles can be distinguished.

$$p = m \cdot c \frac{\beta}{\sqrt{1-\beta^2}} \tag{2.2.2}$$

In the proton-proton collision experiments there was no start detector which could could measure the start time t_0 so that, the time of flight reconstruction was made by using the method of one or more leading particles [2].

Chapter 3

Study of the ppK$^-$ State

Following the theoretical and experimental results explained in section 1, an analysis of the HADES data has been carried out to study how the signature of the ppk- state could be extracted. Before studying the experimental data, the feasibility of the signal reconstruction and the acceptance for the ppK^- events needs to be studied. This section shows the simulations and analysis result for the pure for the ppK^- production, made using the PLUTO event generator and GEANT for the ppK^- bound state.

3.1 Generating a ppK$^-$ with PLUTO

A first simulation of the ppK^- decay was done with PLUTO event generator [7]. Events for the following decay chain have been generated:

$$p + p \longrightarrow K^+ppK^- \tag{3.1.1}$$

The beam energy was set to 3.5 GeV, corresponding to the reaction measured by HADES in 2007. The mass and width of the ppK^- bound state were set to 2.332 GeV/c^2 and 0.06 GeV/c^2 respectively with a mass distribution according to a Breit-Wigner function. The decay channel of the ppK^- into $p\Lambda$ was simulated with a branching ratio of 100%. With this properties a statistics of one hundred milion events were simulated for reaction (3.1.1). The PLUTO simulations were made in order to study the final observables which can also be analyzed in the measured data (e.g. the invariant mass of the $p\Lambda$ pairs and the event kinematics). The PLUTO event generator produces particles according to a phase space distribution and will thus return the ideal kinematics of the four particles in the final state (p_1, p_2, K^+, π^-). Consequently, the $IM_{p\Lambda}$ distribution will exactly correspond to the (MM_{K^+}). In order to reconstruct a ppK^- signal from the simulations, each of the four particles was identified according to the simulated particle identification. The properties of the Λ particles were calculated with the sum of the 4-momentum of the second proton and the π^-. The invariant mass of this sum should correspond to the Λ nominal mass if the proton and π^- stem from the Λ decay. The $IM_{p\Lambda}$ was then calculated by

adding the four-momenta of the two outcoming protons and the π^- and the resulting distribution is shown in fig. 3.1. A Gauss function (red curve) was fitted to the mass distribution, giving a mean value of 2332.0 MeV/c^2 and a width of 29.8 MeV/c^2, which corresponds to the simulated ppK^- properties[1].

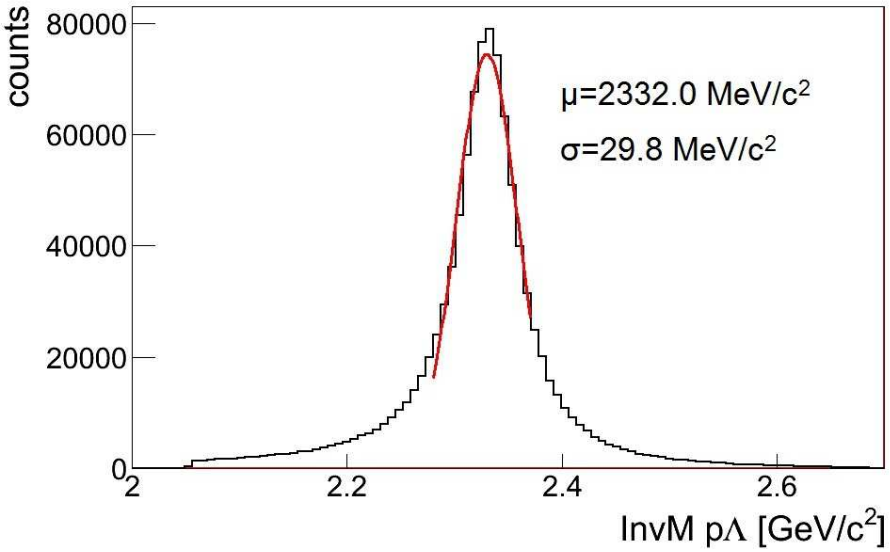

Figure 3.1: IM$_{p\Lambda}$for ppK^- using PLUTO simulator

3.2 Reconstructed Kaonic Clusters inside HADES

To study the geometrical acceptance of the HADES detector to the ppK^- events and the influence of this acceptance on the measured observables, the simulated events of reaction (3.1.1) were processed through a GEANT package [18]. In this way, the detector's response to the traversing particles is modeled properly. A particle is considered to be in the HADES acceptance when traversing all 28 layers of the MDC wire planes. To reconstruct a signal from the ppK^- production, its final decay products (p_1,p_2,π^-) have to be detected with the HADES spectrometer. First, the π^- and p were combined in order to reconstruct the intermediate Λ hyperon. To constrain the analysis to events where a Λ was produced, the invariant mass of the p_2 and π^- (IM$_{p\pi^-}$). The following selection cut was applied to the IM$_{p\pi^-}$:

[1] Note this is a Gauss fit, while a Breit-Wigner function was used to generate the ppK^- state in the simulations.

$$1109\ \text{MeV}/c^2 < \text{IM}_{p\pi^-} < 1120\ \text{MeV}/c^2$$

Afterwards, the reconstructed Λ was combined with the second proton (p_1). In addition, the analysis was selected those events where the K^+, produced together with the ppK^-, was also emitted in the HADES acceptance. The mass distribution of the combination of p_1,p_2,π^- is shown in fig. 3.2.

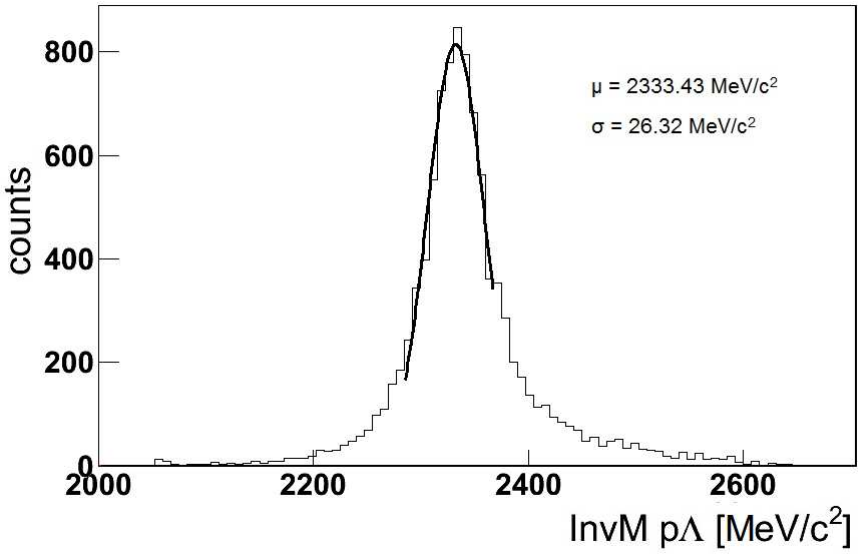

Figure 3.2: IM$_{p\Lambda}$ for the simulated ppK^- events after GEANT, when all four particles (p_1,p_2,π^-, K^+) where inside the HADES acceptance.

The reconstructed ppK^- signal, which corresponds to fig. 3.2 was fitted with a Gauss, which describes the ppK^- signal (black curve). The values for the fitted Gauss function are:

$$\mu = 2334.44\ MeV/c^2$$
$$\sigma = 26.7\ MeV/c^2$$

One should notice that the values from the Gauss fit after running the GEANT simulation are not the same as after running the PLUTO simulation. This difference between both simulations is due to the resolution of GEANT after reconstructing the reaction.

Another part of the analysis focuses on the Dalitz plot. The so called Dalitz plot of a three body production such as:

$$a \rightarrow b + c + d \tag{3.2.1}$$

is obtained by a 2-dimensional representation using the invariant mass squared of two daughter particles ($IM^2{}_{bc}$) on the x-axis and the invariant mass squared of one of the particles just used and the left daughter particles ($IM^2{}_{cd}$) on the y-axis. Both axis will be correlated, as one of the particles (c) appears in both combinations. With a Dalitz plot one can obtain detailed information about structures that will appear in the projected observables. If the projection of one of the Dalitz plot axis shows a peak, the Dalitz plot can help to determine if it is due to a resonance structure that will correspond to a band in the Dalitz plot.

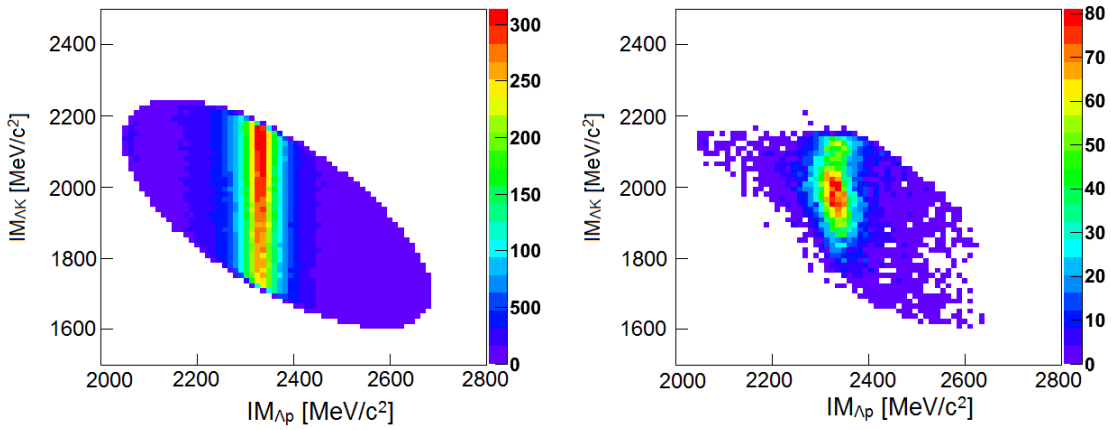

Figure 3.3: Dalitz Plot ($IM_{p\Lambda}$- $IM_{\Lambda K^+}$) for the ppK^- simulation analyzed after GEANT. Left: All statistics. Right: Events where all four particles are inside the HADES geometry.

The Dalitz plot ($IM_{p\Lambda}$ -$IM_{K^+\Lambda}$) for the studied simulation is shown in fig. 3.3.

Note that the Dalitz plot used in this whole project do not use the $IM^2{}_{p\Lambda}$ $IM^2{}_{K^+\Lambda}$ (squared) but the direct observables, as for the DISTO analysis [24]. A vertical band due to the ppK^- bound state can be seen, which will be reflected as a peak in the $IM_{p\Lambda}$, as just explained. The left panel of fig. 3.3 corresponds to all simulated events, while the right panel corresponds to the events where all particles (p_1,p_2,π^- and K^+) are inside the HADES acceptance processed through GEANT. The right panel 3.3 of shows less statistics than the left one, but a band corresponding to the mass of the ppK^- bound state is still visible.

3.2.1 Phase-space distributions

The rapidity and transverse momentum (p_T) are also studied for each of the particles. The rapidity is defined as:

$$y = \frac{1}{2} ln \left(\frac{E + cp_z}{E - cp_z} \right)$$

The advantage of using the rapidity as a description of the particle's kinematics is that applying a boost in the z-direction just adds a constant to the rapidity. In this way, results from experiments with different beam energies can be easily compared. The transverse momentum is defined as:

$$p_T^2 = p_x^2 + p_y^2$$

It is an important quantity, as it gives only the momentum component that the particles retrieved from the collision. The p_z component of the particle's momentum is dominated by the initial beam momentum.

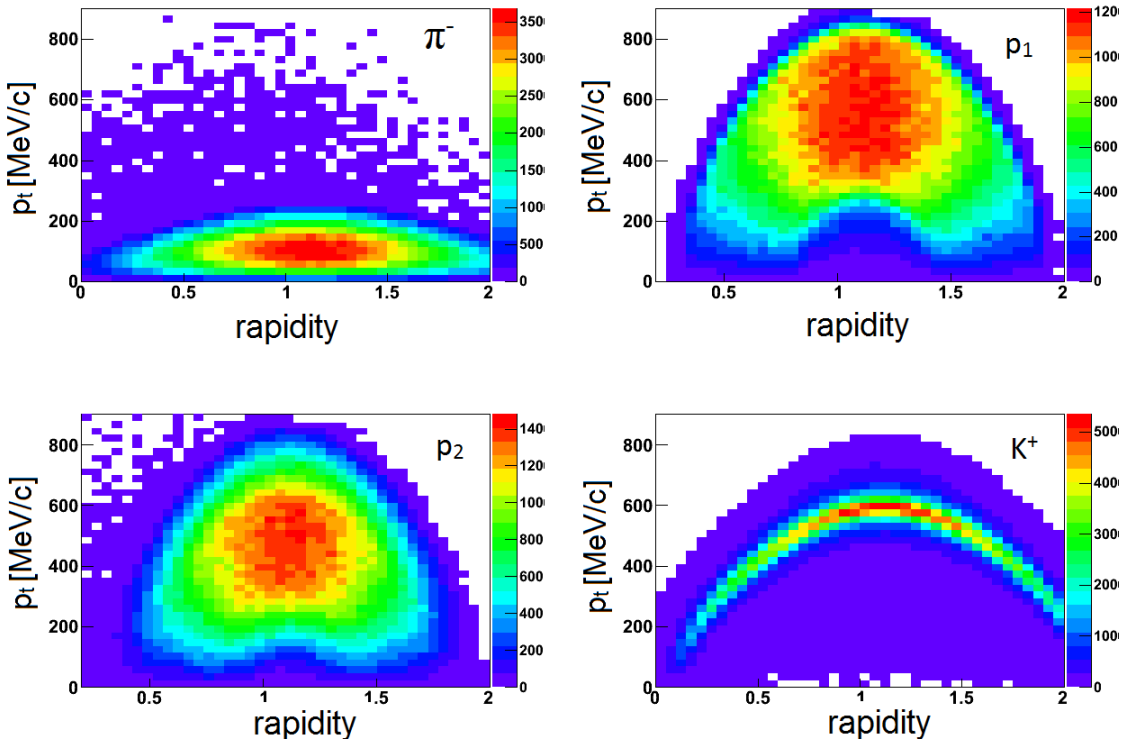

Figure 3.4: Rapidity - Transverse momentum for: π^- (up, left) , proton from the ppK^- decay(up, right), proton from the Λ decay (down, left), K^+(down, right).

Figure 3.4 shows the p_T vs. rapidity distribution of the pion, proton$_1$, proton$_2$, and the K^+ from reaction (3.1.1).

The plots for both fig. 3.4 and 3.5 have been made after running the GEANT program. The four particles were identified using their PID information from the PLUTO simulation. The two protons (p_1, p_2) were distinguished by the information of their mother particle PID.

The rapidity distribution of all four particles is symmetric around 1.118. The pion shows a very low transverse momentum. The two protons show a very broad p_T distribution. The kaon's p_T is a narrow, sickle-like distribution. This special distribution appears due to the limited kinematics, as the kaon in reaction (3.1.1) is produced in a two body decay. The kinematic properties of these type of reactions will be explained in section 4.

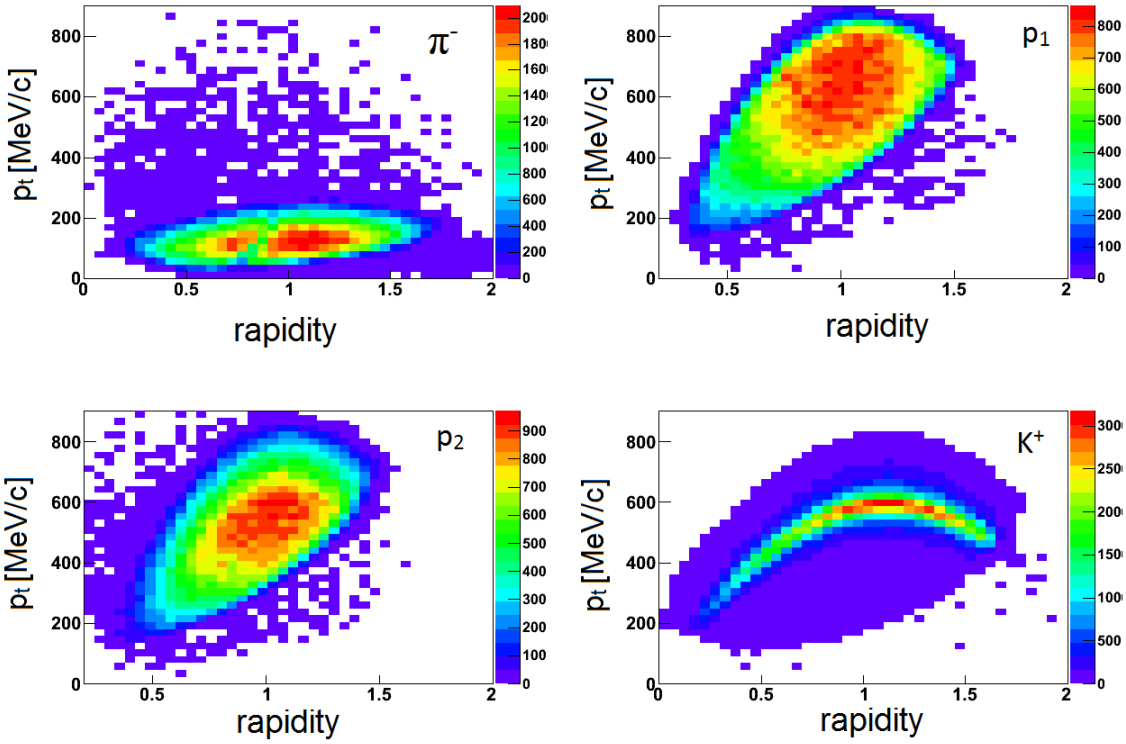

Figure 3.5: Rapidity - Transverse momentum distribution for events where the displayed particle was emitted into HADES acceptance. π^- (up, left) , proton from the ppK^- decay(up, right), proton from the Λ decay (down, left), K^+(down, right).

Figure 3.5 shows the same observable for each one of the four final particles under the condition that it was emitted into HADES acceptance. One can see that the detector acceptance excludes low p_T particles combined with a high rapidity. This is exactly where the 18^o in the θ defines the lower edge of the HADES acceptance.

The one-particle acceptance in the phase space can be retrieved dividing fig. 3.4 by fig. 3.5. The division spectra is shown in fig. 3.6. One can see that the acceptance is rather flat and does not introduce structures.

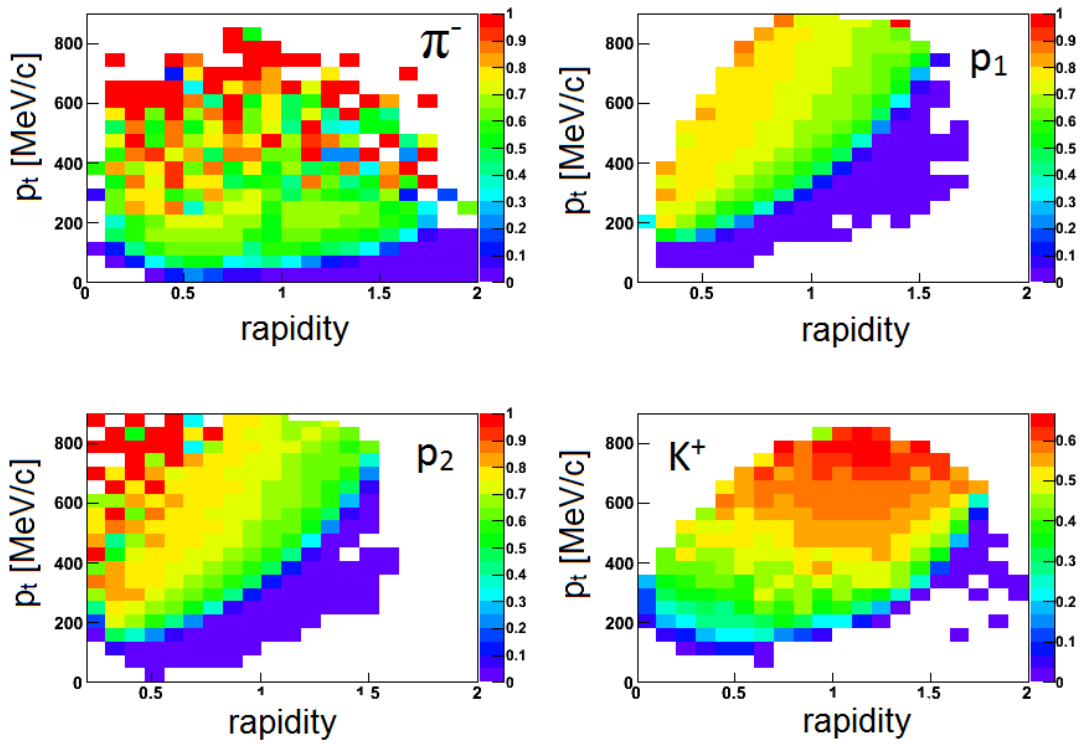

Figure 3.6: Rapidity - Transverse momentum division spectra (particles in acceptance/all particles). π^- (up, left) , proton from the ppK^- decay(up, right), proton from the Λ decay (down, left), K^+(down, right).

Table 3.1 summarizes the acceptance of events with a production of a kaonic cluster. The acceptance was obtained with the help of the GEANT simulations by counting the number of events left over after a certain selection and compare it with the total amount of simulated events.:

$$Acceptance = \frac{N_{selection}}{N_{total}} \tag{3.2.2}$$

The first acceptance was determined by selecting all three decay products of the ppK^- to the HADES acceptance. The second acceptance was determined by selecting all four particles to the HADES acceptance.

If three particles are asked to be in acceptance with the detector's geometry (two protons and π^-) the final number of events is 4.3% from the initial produced events. If four particles are asked to be in acceptance (two protons , K^+ and π^-) the final number of events is 1.3% from the total number of simulated events.

Selection	Acceptance events[%]
p_1, p_2, π^-	4.3
p_1, p_2, π^-, K^+	1.3

Table 3.1: Summary of the acceptance events depending on the particles in acceptance with the detector's geometry.

Chapter 4

Study of possible background channels

The production of a ppK^- out of a proton-proton collision leads to a K^+, proton and a Λ in the final state, as shown in reaction (3.1.1). There are however more prominent sources for the production of these three particles in the final state. These sources result into a background overlaying to the kaonic cluster signal.

In this chapter the characteristics of possible background contributions are analyzed systematically using simulations. The first channel is the direct $pK^+\Lambda$ production

$$p + p \rightarrow pK^+\Lambda \tag{4.0.1}$$

from the proton-proton collision. Another way of producing these three particles is via the excitation of an intermediate N*-resonance. The reaction chain looks as follows:

$$p + p \longrightarrow N^* + p \tag{4.0.2}$$

The N* decay product is K^+ and Λ. The COSY-TOF collaboration recently published data from $p+p$ reactions at four different beam energies [17]. They have studied the exclusive $pK^+\Lambda$ production aiming to determine the contributions from intermediate N* -resonances and final state interactions. The conclusion drawn from these results is that the direct production of $pK^+\Lambda$, compared to the production via an intermediate N*-resonance, is suppressed by one order of magnitude. The main contribution was found to be stemming from the N*(1650)$^+$, N*(1710)$^+$ and N*(1720)$^+$ resonances. As the HADES beam energy is higher, N*-resonances with higher masses are expected to contribute to the final $pK^+\Lambda$ state. The reaction (4.0.2) was this simulated assuming four different masses and widths for the N*-resonances. The values are summarized in table 4.1[1]:

[1]Existence certainty for each $N^* \rightarrow \Lambda K^+$ production. *** Existence ranges from very likely to certain; ** Evidence of existence is only fair.

N* Mass [MeV/c^2]	1650	1710	1800
N* width [MeV/c^2]	165	200	100
PDG evidence	***	**	-

Table 4.1: Masses and width used for N*-resonances. Extracted from PDG particle data. The N*(1800)$^+$ was implemented by hand.

The production of $pK^+\Lambda$ via reaction (4.0.1) and (4.0.2) were simulated with PLUTO using the properties in table 4.1.

Figure 4.1 shows the IM$_{p\Lambda}$ resulting from the PLUTO simulator for reaction (4.0.1) and (4.0.2) assuming three different N* masses. The mass distribution for the simulated reaction (4.0.2) is not symmetric anymore between 2 and 2.7 GeV/c^2 energy like the phase space distribution but it is shifted according to the mass of the simulated N* resonance. The mass distribution for the lightest N* even show a peak around 2.6 GeV/c^2. The pink line in fig. 4.1 corresponds to the pK$^+\Lambda$ channel, which shows a homogeneous phase-space distribution, as it is a direct three-body production. The histograms for the three N*-resonance masses show a peak above 2.4 GeV/c^2, and if one compares this distribution with the invariant mass shown in fig. 3.1 for the decay of the ppK^- state, there, a maximum around 2333 MeV/c^2 is observed which lies fairly below the N* contribution. Hence we infer that looking at the pure kinematic of the events the ppK^- could be separated from the N* contribution by selecting the IM$_{p\Lambda}$.

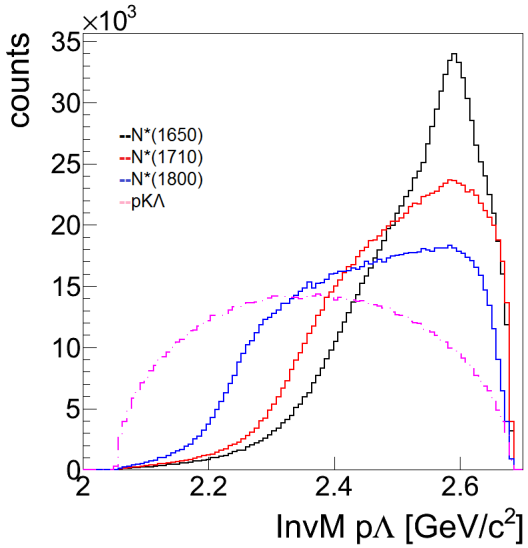

Figure 4.1: IM$_{p\Lambda}$ distribution obtained from PLUTO simulations for N* (1650) [black],N* (1710) [red], N*(1800) [blue] from reactions (4.0.2) and (4.0.1) [pink].

4.1 $pK^+\Lambda$ channel

As explained above, it is important to understand other possible channels leading to the same final state as the ppK^- as they may contribute to the final signal. The direct decay channel $pp \to pK^+\Lambda$ was studied with the same analysis routine as for the ppK^- channel. Figure 4.2 shows the $IM_{p\Lambda}$ produced by the PLUTO event generator. It shows a homogeneous distribution of the $IM_{p\Lambda}$, as expected from a uniform population of a three-particle phase-space.

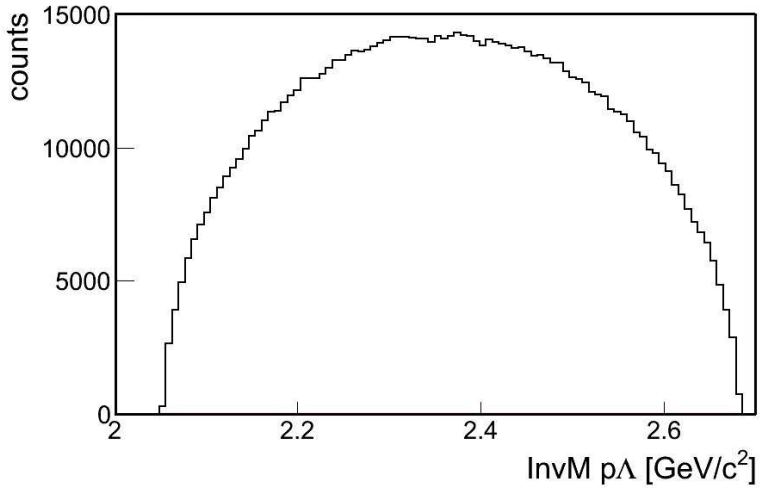

Figure 4.2: $IM_{p\Lambda}$ from the PLUTO simulation for the direct $pK^+\Lambda$ production.

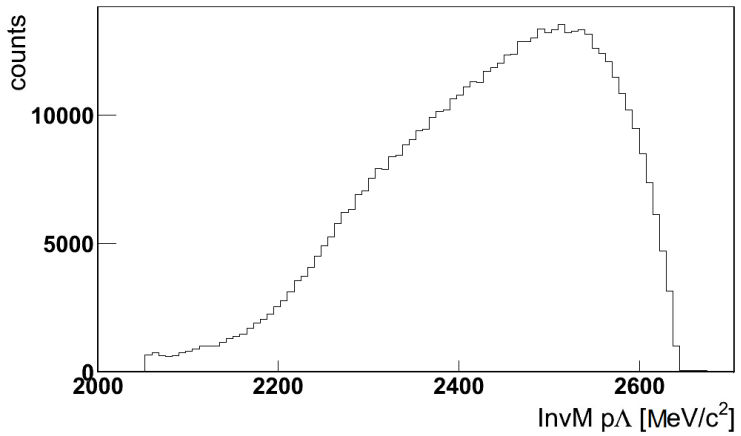

Figure 4.3: $IM_{p\Lambda}$for the direct $p\Lambda K^+$ decay after running the events obtained from the PLUTO simulation through GEANT. All the particles in the final state (p_1, p_2, π^-, K^+) are required to be in the detector acceptance.

Figure 4.3 shows the IM$_{p\Lambda}$ after filtering the simulation through the GEANT program. The contribution of low IM$_{p\Lambda}$ has been significantly reduced by constraining the analysis to particle tracks inside the HADES acceptance only. After this selection is applied, comparing fig. 4.2 with 4.3 one can see that the maximum of the Λp mass distribution is shifted to higher masses.

For a better understanding of the phase space population the statistical distribution in the Dalitz plot was investigated. The Dalitz plot was created by drawing the IM$_{p\Lambda}$ vs. IM$_{K^+\Lambda}$ (fig. 4.4). The left hand panel contains all the simulated events whereas the right panel of fig. 4.4 shows the Dalitz plot for events where the p_1, p_2, π^- *and* K^+ were traversing the HADES detector.

The detector acceptance decreases the statistics in extended regions of the Dalitz plot, creating two diagonal bands, as it is visible in the two green areas in the right panel of fig. 4.4. The geometrical configuration of the HADES spectrometer leads to a high acceptance for the protons flying to the forward direction at the ΛK^+ center of mass [1]. Figure 4.5 shows the angular correlation between the proton and Λ at the ΛK^+ CM. A visible high contribution of angles under -90^o (events with $\theta < -90^o$ correspond to the proton is flying to the forward direction and the Λ flying in the backward direction at the ΛK^+ CM), produced due to the HADES geometry.

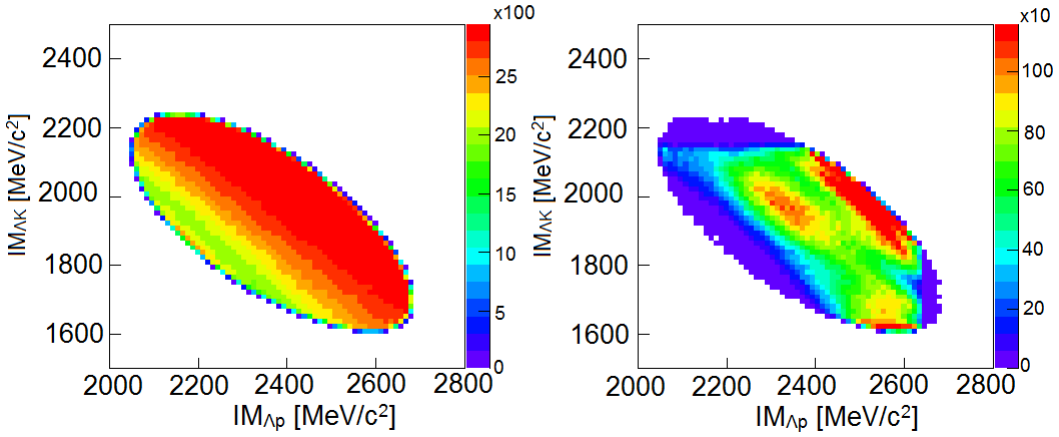

Figure 4.4: Dalitz Plot (IM$_{p\Lambda}$- IM$_{\Lambda K^+}$) for the direct $p\Lambda K^+$ decay after running the simulation through GEANT. Left: All statistics. Right: All particles in acceptance with the detector's geometry.

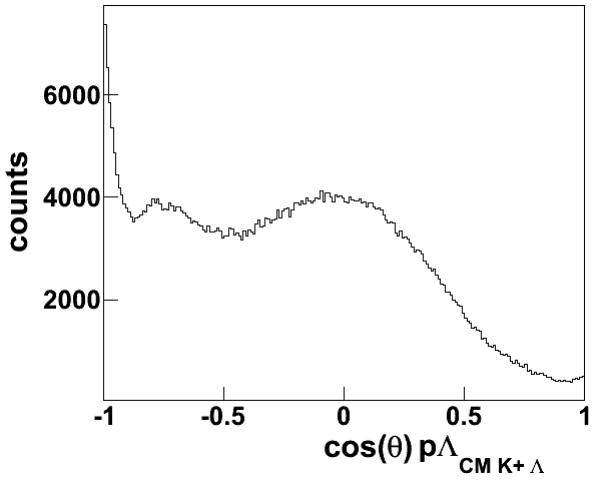

Figure 4.5: $\theta_{p\Lambda}^{CM\ \Lambda K^+}$ after asking all particles to be inside the HADES detector acceptance.

4.2 N* Resonances as background

In the previous subsections, the $\mathrm{IM}_{p\Lambda}$ for the ppK^- and channel 3.1.1 was plotted (fig. 3.2 and 4.3). Since the N* resonances can decay in ΛK^+, the final product of a proton-proton collision producing an N* can lead to the same final products as reactions (3.1.1) and (4.0.2). Due to the same final state as in the ppK^- decay, this reaction is a candidate for background overlaying this signal.

When studying possible background reactions such as (4.0.24.1), one encounters special kinematics which lead to non-uniform distribution of mass observables. This was already visible in fig. 4.1 where one could see that the presence of the N*-resonance decaying into the $K^+\Lambda$ channel also modifies the $\mathrm{IM}_{\Lambda p}$ distribution. This phenomena is known under the name of kinematic reflection. If two particles are produced out of an initial collision the following relation holds:

$$P_M = P_{D1} + P_{D2} \tag{4.2.1}$$

where P_M represents the 4-momentum of the mother particle and P_{D1}, P_{D2} the the 4-momentum for each daughter particle. This condition is the reason why the produced particles maintain a constrained kinematic. This can be shown by the following argumentation:

$$P_{D2}^2 = P_M^2 + P_{D1}^2 - 2P_{D1}P_M \tag{4.2.2}$$

$$m_{D2}^2 = m_M^2 + m_{D1}^2 - 2(E_M E_{D1} - \vec{p}_M \vec{p}_{D1}) \tag{4.2.3}$$

where m_M, m_{D1} and m_{D2} are the masses of the mother and the two daughter particles; E_M, E_{D1} and E_{D2} are the energies of the mother and the two daughter particles. As the masses of the particles are constant values eq. (4.2.3) expresses the connection of the energy of the mother particle and the energy of the produced daughter particles. To simplify this expression we can write it in the rest-frame of the mother particle. This changes the energies and momenta of the equation and leaves the masses invariant. In the rest-frame of the mother particle (RFM) the following properties are fulfilled:

$$\vec{p}_M^{RFM} = 0$$

$$E_M^{RFM} = m_M$$

where$\vec{p}_M^{RFM}$ and E_M^{RFM} are the momentum and the energy of the mother particle at rest. Thus we can write:

$$m_{D2}^2 = m_M^2 + m_{D1}^2 - 2m_M E_{D1}^{RFM} \tag{4.2.4}$$

$$E_{D1}^{RFM} = \frac{m_M^2 + m_{D1}^2 - m_{D2}^2}{2m_{Mother}} \tag{4.2.5}$$

it can also be shown that the absolute value of the momentum value for daughter 1 will be:

$$\left|\vec{p}_{d1}^{RFM}\right| = \frac{[(m_M^2 - (m_{D1} - m_{D2})^2)(m_M^2 - (m_{D1} + m_{D2})^2)]^{1/2}}{2m_M} \tag{4.2.6}$$

In a two body decay, the energy and absolute value of the momentum of the daughter particles are thus well determined at the rest frame of the mother particle. When one applies a Lorentz transformation to a new reference system on the 4-momentum of the daughter particle, the transformed momentum is not expected to be well determined any more.

If reaction (4.0.2) is studied, the proton-proton collision will produce two particles, proton and N*. As this is a two body production, the N* and the proton will have a well determined energy and momentum at the proton-proton center of mass system (CMS). At the rest frame of the N* resonance its two decay products fulfill the same kinematics and will thus also have a well defined energy and absolute momentum. In order to combine the p and the Λ four-momentum to obtain their invariant mass, one has to transform the Λ kinematics from the N* rest frame to the *pp* CMS. If one applies a Lorentz transformation of the N* decay products from the N*-resonance rest frame to the *pp* CMS (eq. (4.2.8)), the absolute value momentum are not well defined any more. The following argumentation will show that also after a Lorentz transformation, the unique original momentum will not be arbitrary distributed. The Λ vector can be parametrized in a parallel and longitudinal component with respect to the flight direction. These two components behave under Lorentz transformation as follows:

$$p_{\Lambda\perp}^{CM} = p_{\Lambda\perp}^{RFM} \tag{4.2.7}$$

$$p_{\Lambda||}^{CM} = \gamma_{N^*}(p_{\Lambda||}^{RFM} - \beta_{N^*} E_{\Lambda}^{RFM}) \tag{4.2.8}$$

where $p_{\Lambda||}^{RFM}$ represents the momentum component of the Λ particle at the N* resframe in the direction of the Lorentz transformation direction, β_{N^*} is the beta factor for the transformation and γ_{N^*} is the gamma factor for the N* and $p_{\Lambda\perp}^{RFM}$ represents the momentum component perpendicular to the Lorentz transformation, which remains invariant under the transformation.

Equation (4.2.8) shows that, the larger the energy of the particle in the RFM is, the larger will the difference of $p_{\Lambda||}^{RFM}$ and $p_{\Lambda||}^{CM}$ be. The energy of the decay particle in the RFM depends, according to eq. (4.2.5), mainly on the mass of the mother particle. In the case of reasonably small mother mass, the particles will have almost no energy in the RFM and thus, the Lorentz transformation will not smear the initial momentum too much. This means that, after the Lorentz transformation, the energy or momentum plot in a new reference frame will still give a peak. The peak will be wider the higher the mother particle's mass is.

If the 4-momenta of the Λ and the proton are summed at the proton-proton center of mass, two vectors with constrained kinematics are summed and thus a mirror peak could appear.

$$\begin{pmatrix} E_p^{CM} \\ \vec{p}_p^{\,CM} \end{pmatrix} + \begin{pmatrix} E_\Lambda^{CM} \\ \vec{p}_\Lambda^{\,CM} \end{pmatrix} = Mirror\ peak$$

This means that when one builds up the invariant mass constructed using the Λ from N* decay and the directly produced proton, a peak appears. These peaks, which appear not because of the direct decay of a particle/resonance into the two analyzed particles (p and Λ) but due to kinematics effects, are known as mirror peaks or kinematic reflection. This effect was studied with help of PLUTO simulations.

4.2.1 Study of the kinematic reflection

The reaction (4.0.2) is a two-body production with a subsequent two body decay and thus mirror peaks may appear in final observables. Investigating, for example, the mass distribution of $\mathrm{IM}_{p\Lambda}$ should not show a peak, as no resonance in the $p\Lambda$ was produced. Despite the p and Λ do not have a common mother particle, fig. 4.1 shows a peak, which corresponds to a kinematic reflection. Simulating events, as in the previous section, for N* resonances and applying the same analysis, might show if the mirror peaks and the ppK^- signal may be distinguished.

The aim of the following PLUTO simulation is to determine if the kinematical reflection of the N*-resonance production might be mistaken for ppK^- signal in the $p\Lambda$ mass distribution.

To study the shape of the kinematic reflections, three different masses for the N* resonances have been used in simulations. The masses and widths for the N*-resonances used in PLUTO are summarized in table 4.1.

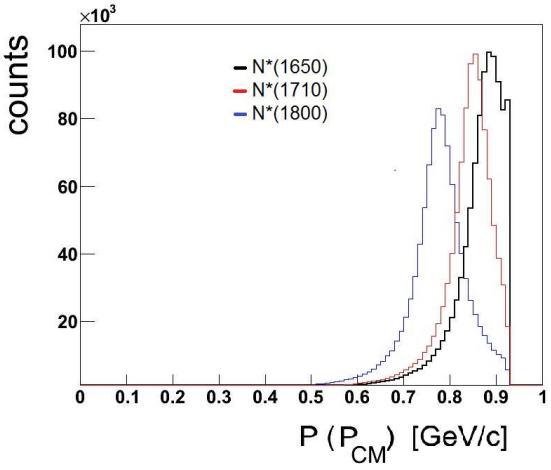

Figure 4.6: Proton (decay particle) momentum at proton-proton center of mass.

Figure 4.6 shows the momentum distribution at the *pp* CM frame for the proton which is produced together with N* (see reaction (4.0.2)) for the three different N* masses. A narrow momentum distribution for each of the three masses is visible, and is consistent with eq. (4.2.6). The broad mass distribution of the N*-resonances is the reason why the proton momentum distribution is not a delta distribution but it is smeared out.

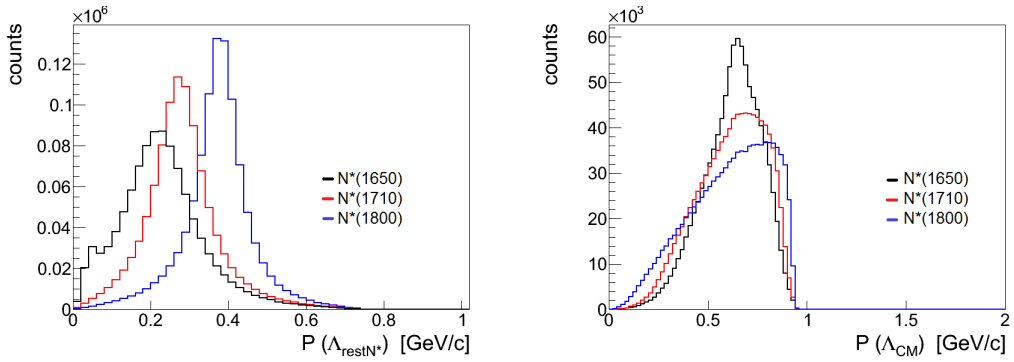

Figure 4.7: (Left panel) Λ momentum at the N* rest-frame. (Right panel) Λ momentum at the proton-proton center of mass. The contribution from the N*(1650), N*(1710), N*(1800) are shown by the black, red and blue histograms respectively.

Figure 4.7 (left panel) shows the momentum distributions of the Λ stemming from the decay of the N* resonances with different masses. As this momentum is calculated in the N* rest frame, the momentum has a narrow distribution for each of the N* masses. The left panel of fig. 4.7 shows the momentum of Λ at the N* rest frame, showing a well determined momentum distribution. The right panel corresponds to the Λ momentum for each of the three simulated N* masses after applying the Lorentz transformation to the p+p CMS. All three momentum distributions show a tendency to higher momentum after the transformation. The higher the N* mass the broader is the peak emerging after the Lorentz transformation. The value for the Λ momentum and the mass over threshold[2] depending ont the N* simulated mass is shown on table 4.2.

The first two N* resonance masses have been extracted from de PDG data [10]. The N*-resonance with mass of 1800 MeV/c^2 is not taken from the Particle Data Group but has been simulated in PLUTO to understand the behavior of the peaks in the final observables depending on the mass of the resonance.

N* mass	Mass over threshold	Λ and K^+ Momentum (N* resftrame)
1650 MeV/c^2	40.6 MeV/c^2	179 MeV/c
1710 MeV/c^2	100.6 MeV/c^2	296 MeV/c
1800 MeV/c^2	190.6 MeV/c^2	380 MeV/c

Table 4.2: Summary of the mass over threshold and momentum of K^+ and Λ at the N* resframe depending on the M_{N^*}.

So far the momentum distribution was shown for all events. However, the detector's acceptance might as well influence the momentum distribution of the particles. Figure 4.8 shows the momentum distribution of the proton and the Λ applying a cut on the θ angle of $15^o<\theta<85^o$ for all particles. This cut gives a good approximation of the HADES detector geometry. After applying the Lorentz transformation (right picture) to the particles' four momenta from the N* rest frame to the proton-proton CMS, the peak is still visible and narrower than before the transformation (left picture).

[2]The mass over threshold is defined as the difference between the mother's particle energy and the sum of the masses of the daughter particles.

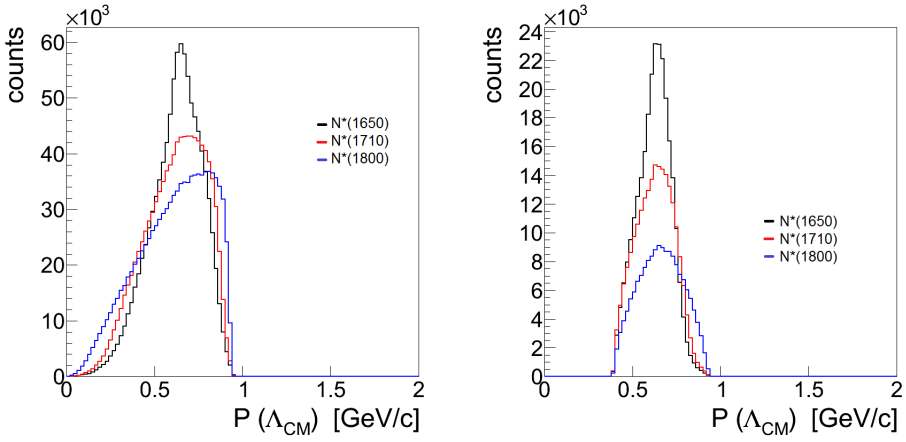

Figure 4.8: (Left panel)Λ momentum at the CM system in full acceptance. (Right panel) Λ momentum with a restriction on θ angle ($15^{o}<\theta<85^{o}$).. The contribution from the N*(1650), N*(1710), N*(1800) are shown by the black, red and blue histograms respectively.

Chapter 5

Full Scale Analysis

In the previous chapter the production of $pK^+\Lambda$ final state through different intermediate decays was discussed. In the experiment not only these channels will be produced, but also many other background channels, which will contribute to the final signal. This chapter shows the simulation of the final signal including different background channels, in order to get a realistic estimation for the feasibility of the measurement of the ppK^- state.

5.1 The ppK$^-$ and the multichannel background

In order to mimic final observables that are similar to the experimental data, the following production channels were included in simulations with a yield according to the quoted cross section. In this way, the background contribution is taken into account.

$K^+p\Lambda(1405)$	$\sigma = 22.35\,\mu b$	(a)
$\Sigma^0(1385)K^+p$	$\sigma = 11.13\,\mu b$	(b)
$K^+p\Lambda\pi^0$	$\sigma = 4.06\,\mu b$	(c)
$K^+p\Lambda$	$\sigma = 48.00\,\mu b$	(d)
$K^+p\Sigma^0$	$\sigma = 25.16\,\mu b$	(e)
$K^+p\Sigma^0\pi^0$	$\sigma = 0.21\,\mu b$	(f)

$K^+p\Lambda(1520)$	$\sigma = 22.97\,\mu b$	(g)
$K^+p\Lambda\pi^-\pi^+$	$\sigma = 0.015\,\mu b$	(h)
$K^+p\Sigma^+\pi^-$	$\sigma = 0.011\,\mu b$	(i)
$K^+p\Sigma^+\pi^-\pi^0$	$\sigma = 7 \cdot 10^{-5}\,\mu b$	(j)
$K^+p\Sigma^0\pi^-\pi^+$	$\sigma = 4.77\,\mu b$	(k)
$K^+\,ppK^-$	$\sigma = 10.00\,\mu b$	(l)

The colors assigned to each final state correspond to the colors used for each channel in simulations. These reaction channels were chosen due to their final states, as all of them contain a proton and a positive Kaon. It is likely that at least some of the reactions (a)-(l) pass the event selection successfully though they do not stem from reaction (3.1.1). The cross-sections of the background channels had been estimated from an independent analysis of the experimental data [3]. The cross-section for the ppK^- channel was assumed to be $10\mu b$ according to some estimation based on a very phenomenological model[23].

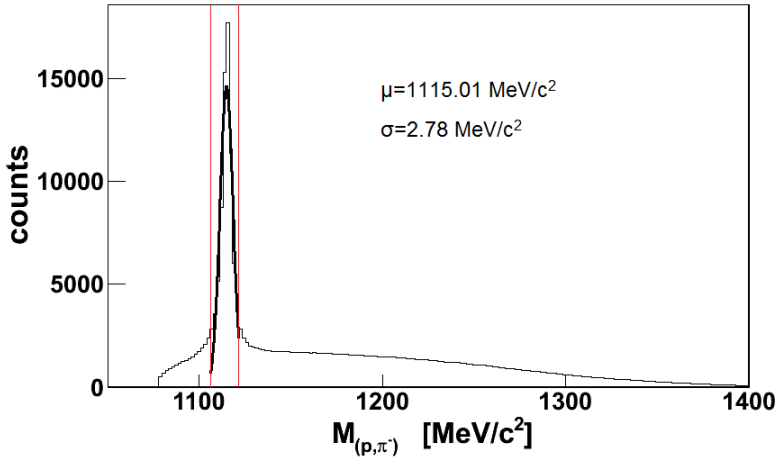

Figure 5.1: IM$_{p\pi^-}$ for the channels (a)-(l). The red line shows the mass cut used in the analysis to select channels containing a Λ hyperon.

On this set of simulation, an analysis for the reconstruction of the ppK^- bound state was applied. The analysis works as follows: the Λ signal is reconstructed by adding the proton and the π^- four-vector and calculating its invariant mass. Figure 5.1 shows the resulting invariant mass. A clear Λ signal is visible overlapped to the combinatorial background. On the IM$_{p\pi^-}$ a cut around the mean value of the Gauss fit of 1.5 σ was applied (1110 MeV/c^2<IM$_{p\pi^-}$< 1119 MeV/c^2). The red vertical lines in fig. 5.1 indicate the applied cut.

The next observable used for the event selection is the mass of the K^+ meson and it is considered to suppress the contribution by misidentified particles. Figure 5.2 shows the reconstructed M_{K^+} for all Kaon candidates (positively charged particles). The contribution from misselected π^+ and protons is also visible in the mass spectrum. To show the signal of the particles separately, particles were selected using their GEANT ID information. Again, the two vertical red lines refer to the applied cut on M_{K^+}(280 MeV/c^2<M_{K^+}<750 MeV/c^2) in order to improve the K^+ purity.

Figure 5.3 shows how the previous cuts change the final MM_{K^+} signal. The black line corresponds to the total simulation whereas the blue and the red histograms show the contribution by the misidentificaiton of protons and pions and the magenta histogram corresponds to the correctly identified kaons. The orange line shows the total signal of the ppK^-. In the next subsection, the number of reconstructed ppK^- depending on the cuts just described was calculated.

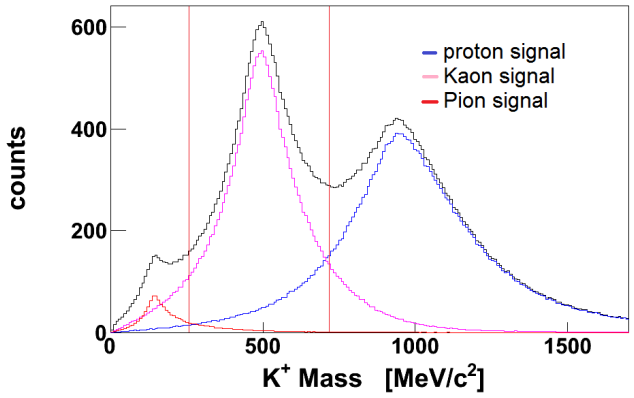

Figure 5.2: Reconstructed M_{K^+} from all channels obtained after a cut on $IM_{p\pi^-}$ is applied. The red vertical lines show the cuts applied to select K^+.

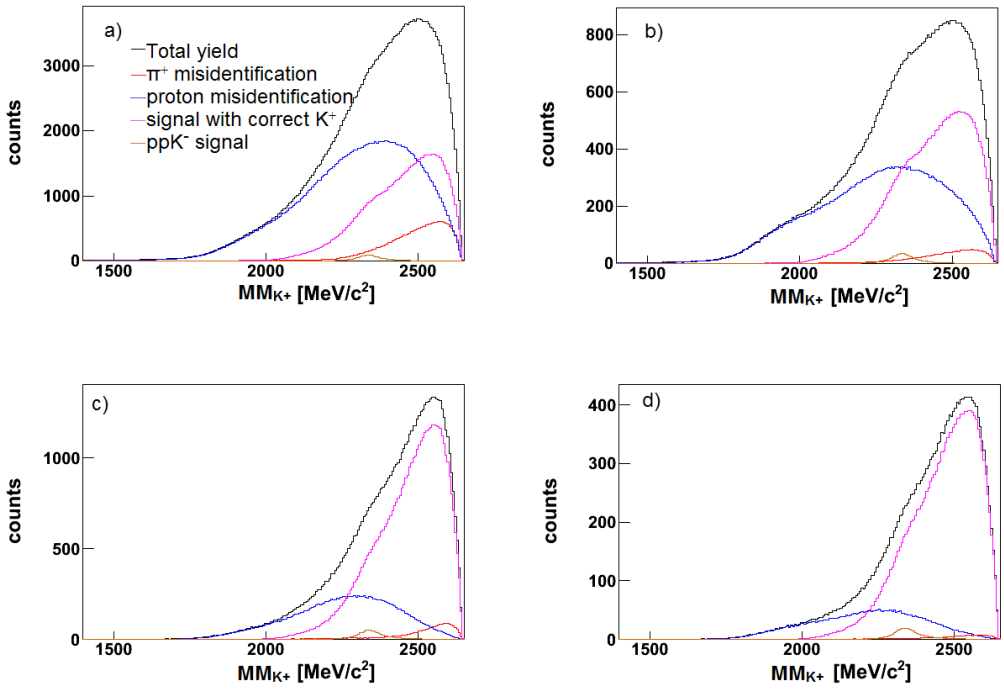

Figure 5.3: Reconstructed $MM_{K^+}$when: a) No cut is applied, b) after the following $IM_{p\pi^-}$ selection: 1110 MeV/c^2<$IM_{p\pi^-}$< 1119 MeV/c^2, c) after the following M_{K^+} selection: 280 MeV/c^2<M_{K^+}<750 MeV/c^2, d) when both M_{K^+} and $IM_{p\pi^-}$ cuts were applied.

The observables which will finally be analyzed are the MM_{K^+} and $IM_{p\Lambda}$ and as it is visible from reaction (3.1.1), these two observables should reflect the mass distribution of the ppK^-. In order to disentangle the different contributions by the different reaction channels, the MM_Λ and MM_{pK^+} are studied. Figure 5.4 shows the four distributions (MM_{K^+}, $IM_{p\Lambda}$, MM_Λ and MM_{pK^+} plotted with black points) together with the contribution of each different channel (a) to (l). The goal is now to optimize the signal to background (S/B) ratio for the MM_{K^+} and $IM_{p\Lambda}$ distributions. In fig. 5.4 the final observables MM_{K^+} and $IM_{p\Lambda}$ are shown. The red curve corresponds to the ppK^- signal. Figure 5.4 a) and b) show the two possible observables which can be used to suppress other reactions with respect to the ppK^- production.

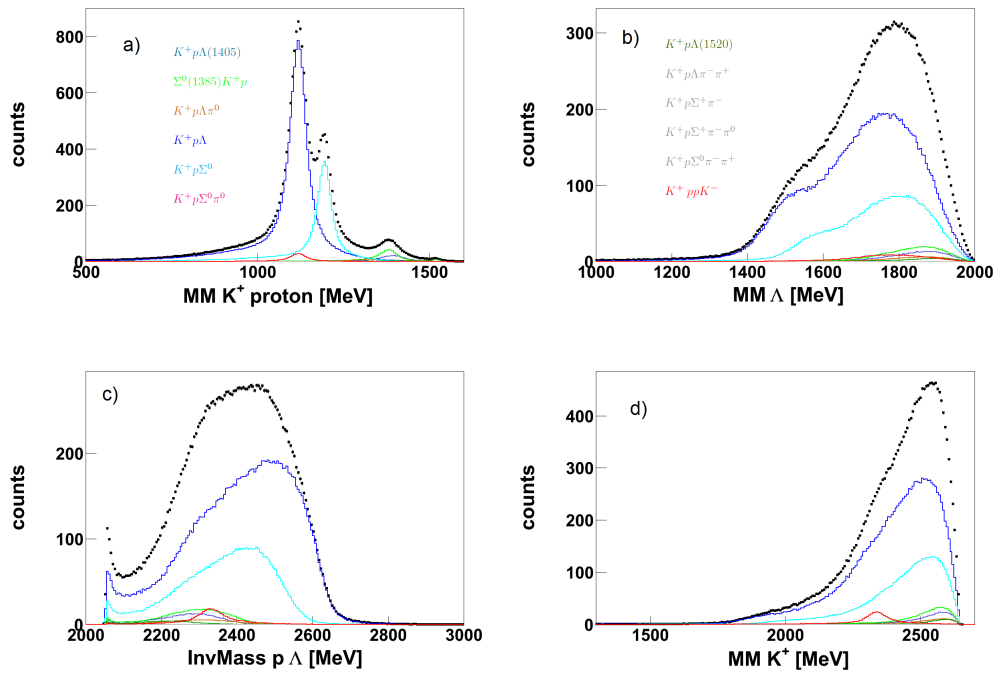

Figure 5.4: Simulated observables with the contribution of each different channel to the final signal. a)MM_{pK^+}, b)MM_Λ, c)$IM_{p\Lambda}$, d)MM_{K^+}.

It can easily be seen, that most of the background channels in the MM_{pK^+} figure deliver the largest contribution to the higher mass range (at MM_{pK^+}>1150MeV/c^2). Selecting this observable to 1000 MeV/c^2< MM_{pK^+}<1150 MeV/c^2 most of the non-interesting channels could be rejected from the analysis. The red lines on the left panel of fig. 5.5 shows the mentioned MM_{pK^+} cut.

If one uses a representation of the yield in a logarithmic scale, like in fig. 5.5, it is obvious that the direct pΛK^+ production (blue) is not separable from a ppK^- production in the MM_{pK^+} distribution. Any cut applied on the MM_{pK^+} to improve the signal to background ratio (S/B) for the ppK^- channel did not improve the ppK^-/pΛK^+ ratio. The only observable in which the ppK^-/pΛK^+ ratio was not constant over the whole mass range was the MM_Λ (fig. 5.5 b)). A second cut was applied on the latter, excluding regions where the ppK^-/pΛK^+ ratio was smaller (1685 MeV/c^2<MM_Λ<1950 MeV/c^2).

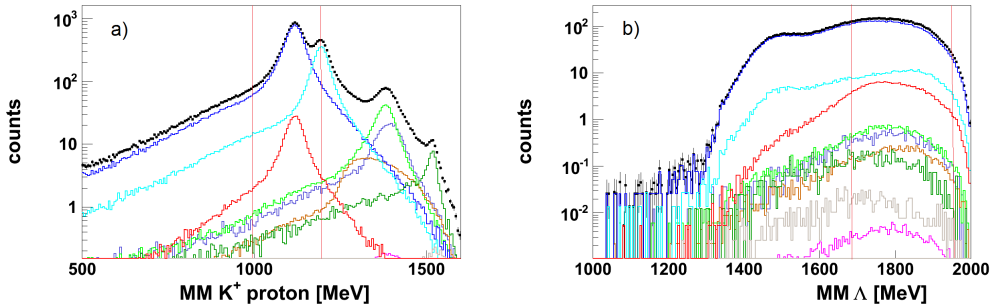

Figure 5.5: Cut applied at 1000 MeV/c^2< MM$_{pK+}$<1150 MeV/c^2 and 1685 MeV/c^2<MM$_\Lambda$<1950 MeV/c^2 (red vertical lines). a)MM$_{pK+}$, b)MM$_\Lambda$, .

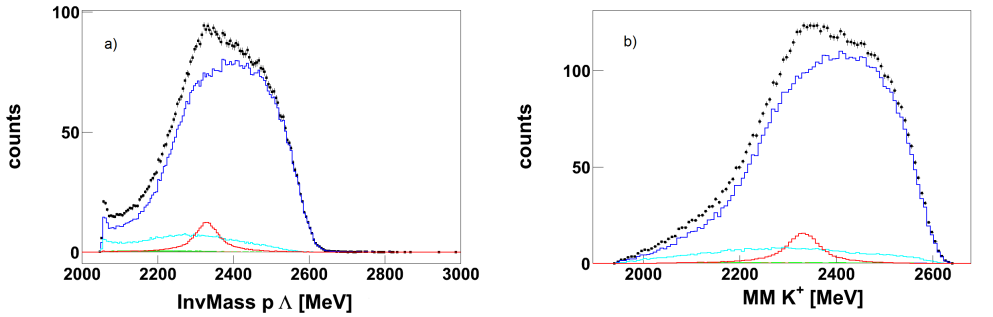

Figure 5.6: Observables with the contribution of each different channel to the final signal with linear scaling. Cut applied at 1000 MeV/c^2 MM$_{pK+}$and 1685 MeV/c^2<MM$_\Lambda$<1950 MeV/c^2 (red vertical lines). a)IM$_{p\Lambda}$, b)MM$_{K+}$

Figure 5.6 shows the two final mass observables, IM$_{p\Lambda}$ and MM$_{K+}$ after the two selection cuts mentioned before. The cut on MM$_{pK+}$ reduces significantly the contribution of the background channels except for the pK$^+\Lambda$ direct production, which is suppressed by applying a selection on the MM$_\Lambda$. The improvement of the S/B ratio is visible when comparing fig. 5.6 with fig. 5.4 as a signal from the ppK^- is now recognizable upon the total signal (black points) of IM$_{p\Lambda}$ and MM$_{K+}$.

5.2 Estimated ppK^- events in HADES

The number of ppK^- which could be reconstructed in experimental data was estimated considering the statistics of p+p collision at 3.5 GeV measured by HADES in 2007. The estimation was done assuming a cross section of 10μb for the ppK^- production in this collision.

Using the following expression, the number of reconstructed ppK^- could be calculated [5]:

$$\frac{N_{ppK^-}}{\sigma_{ppK^-}} = \frac{N_{pp}^{el-acc}}{\sigma_{pp}^{el-acc}} = 1.45 \cdot 10^8 mb^{-1} \tag{5.2.1}$$

where N_{ppK^-} are the number of produced ppK^-, σ_{ppK^-} is the cross-section of the ppK^- production. N_{pp}^{el-acc} are the number of proton-proton elastic collisions in the geometrical acceptance with the detector, and finally σ_{pp}^{el-acc} is the cross section of the latter.

In order to obtain a number of reconstructed ppK^- out of the total produced number of ppK^- clusters, one has to take the acceptance and efficiency into account. This is expressed in eq. (5.2.2).

$$N_{ppK^-} = \sigma_{ppK^-} \cdot \frac{N_{ppK^-}^{el-acc}}{\sigma_{ppK^-}^{el-acc}} \cdot 0.5 \cdot (acc + eff) \cdot 1.6 \tag{5.2.2}$$

Considering σ_{ppK^-}=10μb, $\frac{N_{ppK^-}}{\sigma_{ppK^-}} = 1.45 \cdot 10^8 mb^{-1}$ and an extra correction factor of 1.6, the resulting number of ppK^- states is summarized in table 5.1. A factor 0.5 was introduced as the simulations were made just considering the $p\Lambda$ production for the ppK^-. If no cuts are applied, 3180 ppK^- can be reconstructed. If both $IM_{p\pi^-}$ *and* K^+ cuts are applied, 696 ppK^- can be reconstructed.

CUT	ppK^- in simulation	*S/B*	*ACC&EFF*	ppK^- ***to be measured***
None	*273 350*	*0.1*	*0.27%*	***3180***
$IM_{p\pi^-}$	*103 649*	*0.16*	*0.10%*	***1160***
K^+	*148 128*	*0.23*	*0.15%*	***1740***
$IM_{p\pi^-}$ *and* K^+	*57 110*	*0.26*	*0.06%*	***696***

Table 5.1: Number of events containing ppK$^-$, S/B ratio, acceptance and efficiency, and number of reconstructed ppK$^-$ depending on the applied cut .

5.3 ppK$^-$ and N* resonances

As was discussed earlier, the pK$^+\Lambda$ yield may be also partially due to the production of N^{*+} resonances. Thus, the same analysis as in subsection 5.1 was performed using only the production of N*-p as contribution to the pK$^+\Lambda$ total yield. Three different N* resonances were used for this simulation in order to understand how the cuts affect the observables depending on the mass of each resonance[1]:

N^{*+} Mass [MeV/c^2]	1650	1720	2190
N^{*+} width [MeV/c^2]	165	200	500
PDG evidence	***	**	*

Table 5.2: Masses and width used for N^{*+}-resonances. Extracted from PDG particle data.

As was explained in section 4, the presence of N^{*+}-resonances can cause mirror peaks in the $p\Lambda$ invariant mass spectrum. For the data analysis this fact has to be treated with care, as it can be misunderstood as a signal trace in a $p\Lambda$ decay. One can observe that, in the case of all N^{*+} resonances, a mirror peak appears in the IM$_{p\Lambda}$ spectrum. The width of the mirror peak increases with the N^{*+} resonance mass. Assuming a ppK^- mass of 2.332 GeV/c^2 and width of 0.06 GeV/c^2 for a Breit-Wigner distribution, these mirror peaks will not be mistaken for a ppK^- signal. This, however, has to be inspected closely as so far the mass and the width of the ppK^- state is highly hypothetical.

The yield of the background is the same as the one used in the previous subsection, but the total pK$^+\Lambda$ phase space yield was substituted by events where N^{*+}-p was isotropic produced. Figure 5.7 shows the MM$_{K^+}$ and IM$_{p\Lambda}$ mass distributions under the condition 1110 MeV/c^2<IM$_{p\pi^-}$< 1119 MeV/c^2 and 280 MeV/c^2<M$_{K^+}$<750 MeV/c^2. The three panels correspond to the different N^{*+} resonances with different masses. For each case the extreme assumption is made that the whole $pK^+\Lambda$ yield is associated to the resonant production. These distributions correspond to the case in fig. 5.4 where the background was modeled by the direct pK$^+\Lambda$ production. The left picture in the middle row shows the MM$_{K^+}$ for the N*(1720)$^+$, which behaves very similar to the N*(1650)$^+$ with less contribution for high masses. Finally, the third panel (left lower) shows the MM$_{K^+}$ for N*(2190)$^+$. This figure is completely different from the ones discussed before and shows a similar shape to the direct pK$^+\Lambda$ production (see fig. 5.4).

[1] Existence certainty for each $N^* \rightarrow \Lambda K^+$ production. *** Existence ranges from very likely to certain; ** Evidence of existence is only fair. *Evidence existence is poor.

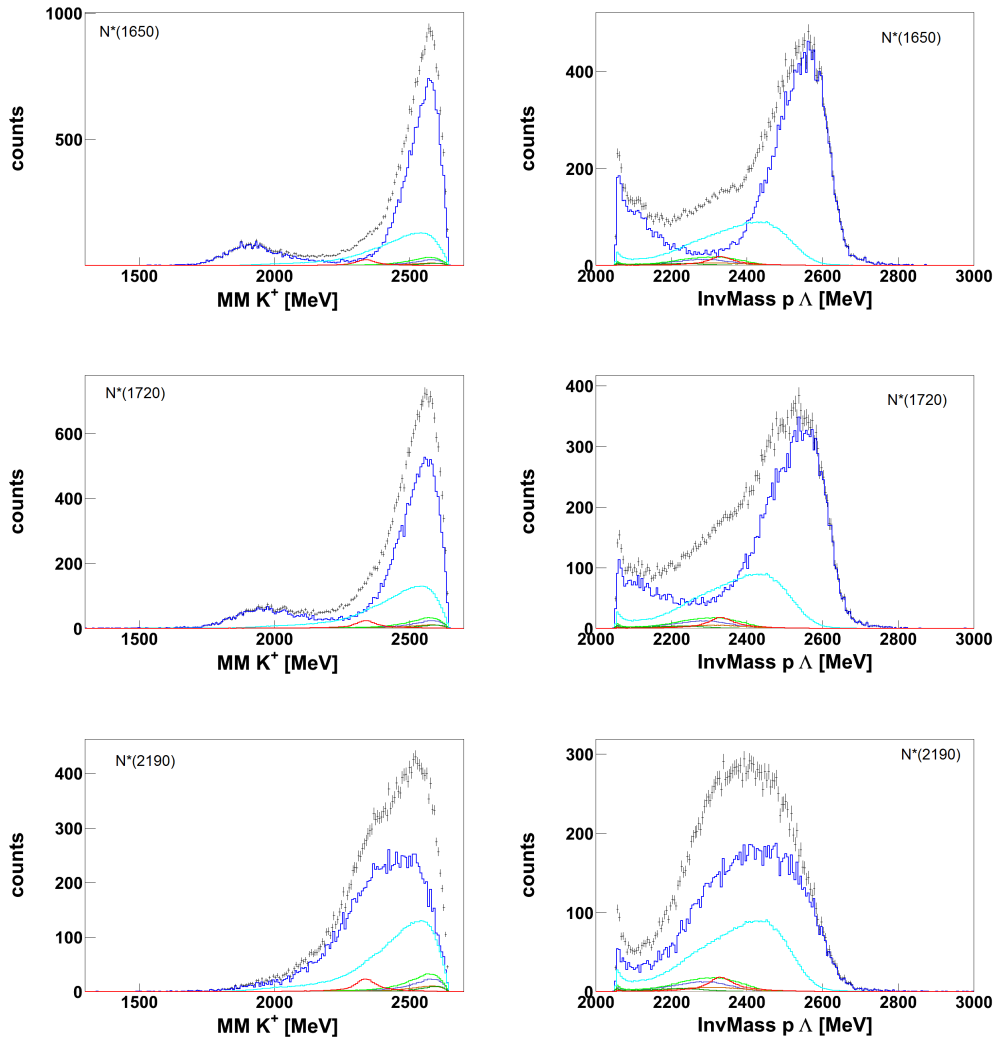

Figure 5.7: MM_{K^+} (left) and $IM_{p\Lambda}$ (right) for the three simulated N^{*+} resonances (from upper to lower: 1650, 1720, 2190).

A further constraint (1000 MeV/c^2< MM_{pK^+}<1150 MeV/c^2) was applied to suppress the contribution of the background channels. As it is shown in fig. 5.8, where the MM_{K^+} and $IM_{p\Lambda}$ spectra after the selection on the MM_{pK^+} are displayed, this selection significantly reduces the contribution by the background channels to the total signal, as it was the case for the direct $pK^+\Lambda$ production.

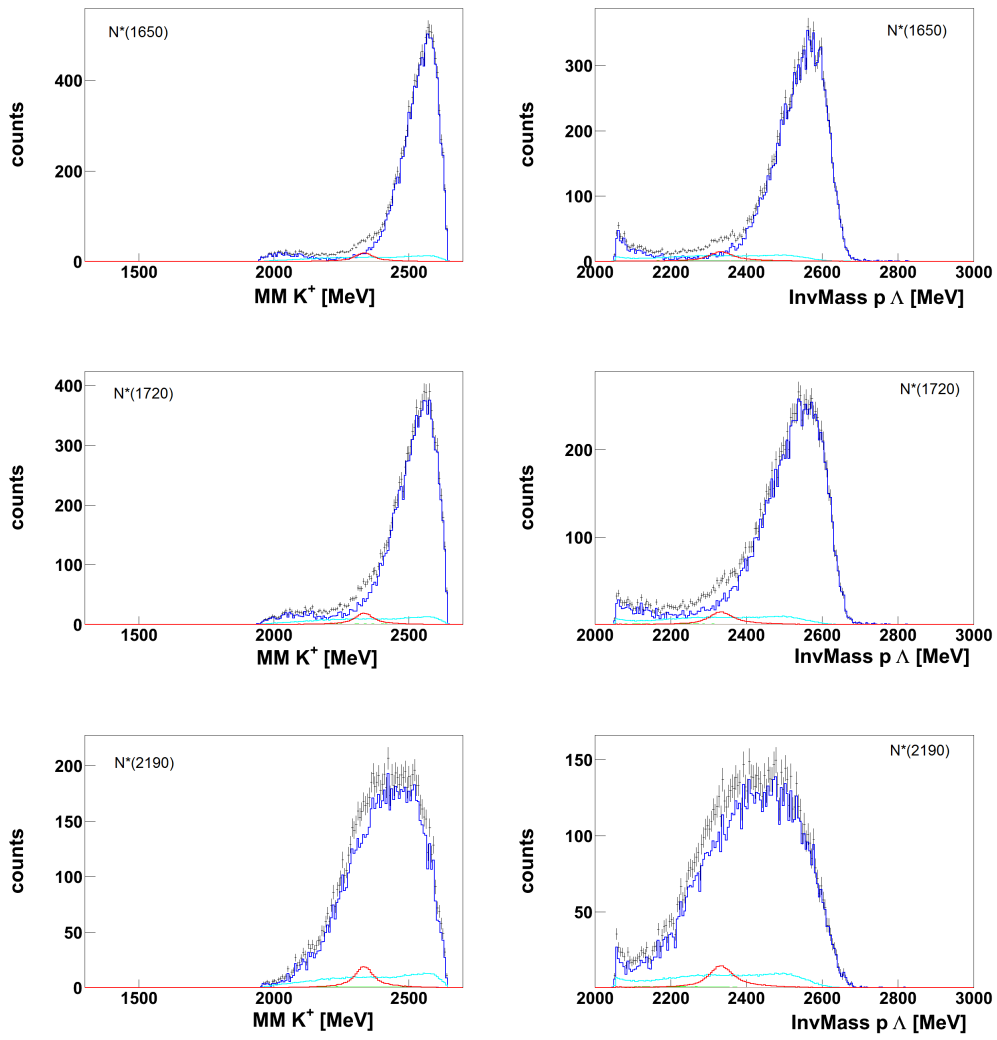

Figure 5.8: MM_{K^+} (left) and $IM_{p\Lambda}$ (right) for the three simulated N*$^+$ resonances (from upper to lower: 1650, 1720, 2190). Cut on 1000 MeV/c^2< MM_{pK^+}<1150 MeV/c^2 is applied.

The selection on the MM_Λ which was used for the the direct $pK^+\Lambda$ production was applied (1685 MeV/c^2<MM_Λ<1950 MeV/c^2) to study its effect upon the N*$^+$ resonances observables. When the second cut was applied, the contribution to the final signal from the N*(1650)$^+$ and N*(1720)$^+$ was considerably reduced (fig. 5.9). In the case in which the background is dominated by N*(1650)$^+$ and N*(1720)$^+$ resonances, the signal of the ppK^- is even more visible than the N*$^+$ signal. In the case of a high mass of the N*$^+$ resonance, the signal overlapped completely

with the signal of a ppK^- bound state with mass 2332 MeV/c^2, as happened with the direct $pK^+\Lambda$ production.

In the measured data, it is probable to have several N^{*+} resonances as a source for the $pK^+\Lambda$ yield, so that these simulations can only serve as a qualitative estimation.

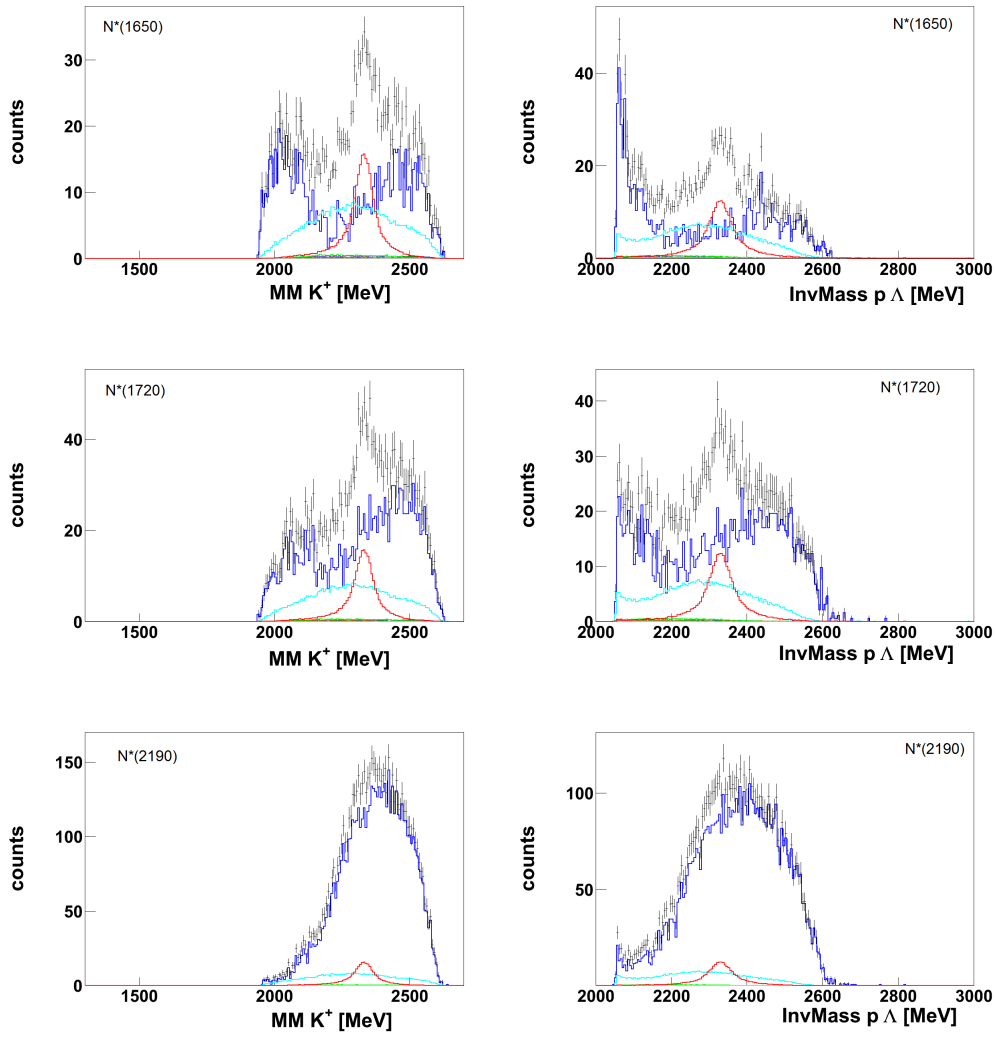

Figure 5.9: MM$_{K^+}$ (left) and IM$_{p\Lambda}$ (right) for the three simulated N^{*+} resonances (from upper to lower: 1650, 1720, 2190). Cuts on 1000 MeV/c^2< MM$_{pK^+}$<1150 MeV/c^2 and 1685 MeV/c^2<MM$_\Lambda$<1950 MeV/c^2 are applied.

5.4 Extraction of the ppK$^-$ signal

When analyzing the experimental data, the real contribution of each channel is not well known and neither is the real mass of a ppK^-. When applying the studied cuts to the data, one has to be careful with the interpretation of the resulting peaks.

In order to extract a signal of the ppK^- from the measured data, one has to know the background in details. There are two possibilities how to unfold the background from the measured spectra. The first consists in subtracting a simulated background from the experimental spectra. The yield which is left over after the substraction could be accounted to a new source. The difficulty in this method lies in a proper scaling of the background to the data. A second method is to divide the experimental data by a simulated background that includes only the phase space distribution of the final products. In this way, a proper scaling is not necessary and every yield which outcomes over a flat deviation spectrum can be accounted to a new signal. In both cases it is however important to model the mass distribution of the background properly. On the other hand, the contributing resonances might overlap and interfere such that the presence of peaks can not always be interpreted in a unique way.

As shown in the previous subsection, the shape of the background depends strongly on the intermediate state that the Λ and the K^+ form. This intermediate state is however not known yet from the analysis of the experimental data. Due to the lack of knowledge, a wrong assumption to model the background can be introduced. Lets assume, for example, that one of the examples shown in fig. 5.9 holds true and the complete $pK^+\Lambda$ yields (apart from the ppK^- contribution) coming from the N^{*+} decay but that the wrong assumption is made and the total spectra are compared to the pure phase space emission of the $pK^+\Lambda$ final state. It is important to check whether the deviation spectra obtained by dividing the distribution shown in fig. 5.9 by the $pK^+\Lambda$ phase space distribution lead to artificial peaks that could be then mistaken by physical signal. This test has been carried out and the results are shown in fig. 5.10.

Figure 5.10 shows the IM$_{p\Lambda}$ (left) and the MM$_{K^+}$ (right) for simulated N^{*+}-resonances with three different masses divided by the distribution obtained simulating the $pK^+\Lambda$ final state emitted according to the phase space kinematic. The upper four histograms (corresponding to masses for the N^{*+} resonances of 1650 MeV/c^2 and 1720 MeV/c^2) show a visible peak for the ppK^- whereas no peak is visible on the lower histograms (corresponding to an N* mass of 2190 MeV/c^2). One can see that the deviation spectrum using a wrong background indeed creates structures. For the $N^*(1650)^+$ and $N^*(1720)^+$ ratios, a convex structure is created, and it shows itself as a rise of the ratio at small and large masses. The scale and shape of these structures are however completely different from the ppK^- signal. The ratio of $N^*(2190)^+$ shows a uniform distribution, which reflects again the similarity between this N^{*+} and the direct $pK^+\Lambda$ production.

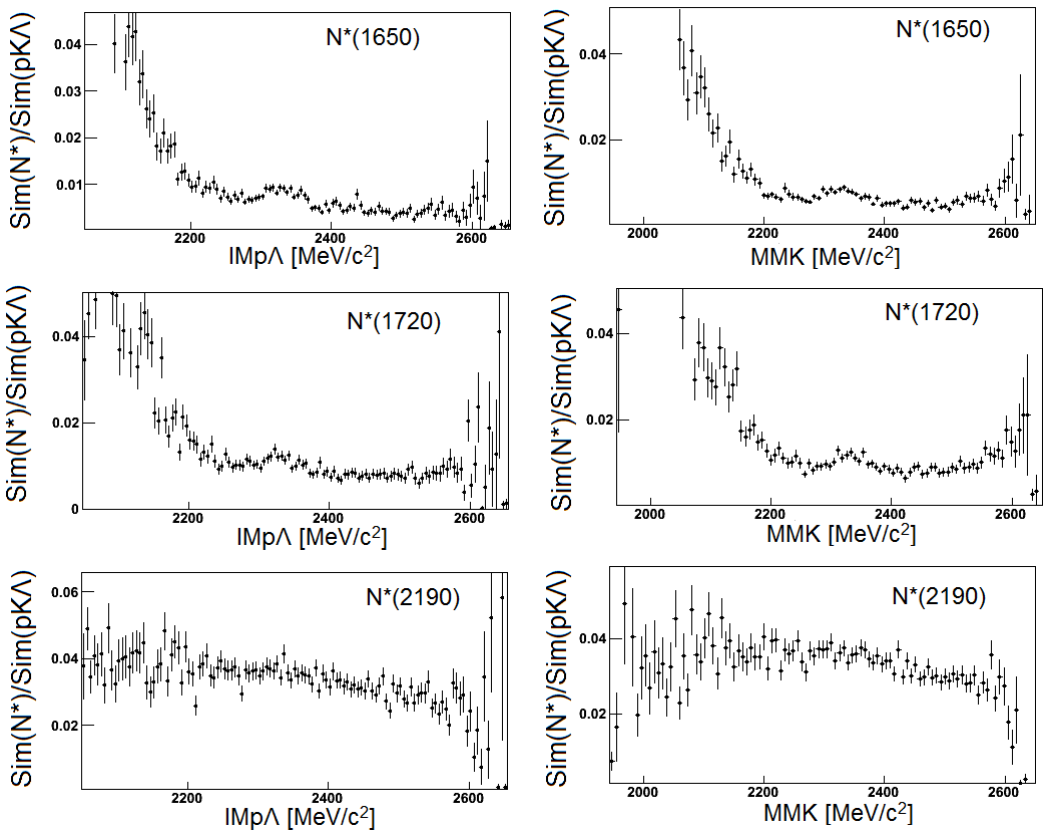

Figure 5.10: Deviation spectra of the $\mathrm{IM}_{p\Lambda}$ (left column) and MM_{K^+} (right column) for the three simulated N* resonances.

Chapter 6

Analysis of the experimental data

As explained in the introductory part of this work, there have already been some publications on ppK^- observations in experimental data[22, 12, 4]. The DISTO collaboration published in 2010 [22] the analysis results for proton-proton collisions at a beam kinetic energy of 2.85 GeV which showed a peak in the $IM_{p\Lambda}$ and MM_{K^+} distributions at 2265 ± 2 MeV/c^2 with a width of 118 ± 8 MeV/c^2. In this section, firsts result of the data analysis taken by the HADES spectrometer are shown.

6.1 Event selection of experimental data

The p+p reaction with a beam kinetic energy of 3.5 GeV on a fixed target was measured with the HADES experiment, $1.2 \cdot 10^9$ events were collected during this campaign. This statistics was analyzed to select events with the $pK^+\Lambda$ final state. The first step of the analysis consists in selecting the two final protons, the positively charged pion and an additional positively charged particle using the dE/dx information (see section 2) and assigning each of the different particles its corresponding PID. After identifying each of the particles, the Λ mass was reconstructed by adding the four-momentum of the identified protons and pions. Events outside the following intervals were rejected:

Observable	Lower cut [MeV/c^2]	Higher cut [MeV/c^2]
$MM_{ppK^+\pi^-}$	-90	35
MM_{pK^+}	1050	1160
$IM_{p\pi^-}$	1106	1122
M_{K^+}	270	700

Table 6.1: Cuts applied on $MM_{ppK^+\pi^-}$, MM_{pK^+}, $IM_{p\pi^-}$ and M_{K^+}.

As discussed in the previous sections, events containing a Λ particle can be chosen by applying a selection cut on the $IM_{p\pi^-}$ and MM_{pK^+} distribution around the Λ nominal mass. As the

interesting events are the ones which have pK$^+\Lambda$ in the final state, the missing mass of the four detected particles (the two protons, the π^- and the K^+) should be distributed around zero, a cut on MM$_{ppK^+\pi^-}$, as shown in table 6.1, was applied. Finally, a cut on the K^+ mass was applied, (see section 5) in order to reduce the contamination by events with a wrong identified kaon.

As the purity of the K^+ identification is rather low, not only events with strangeness were selected with this analysis. There was however a method developed to model this source of the background by a sideband analysis on the Kaon mass (see [8]). The method to subtract the contribution by the misentidfiation is not described here but we show in the following only spectra where this yield has already been subtracted.

6.2 Data description by direct $pK^+\Lambda$ production

The DISTO collaboration analyzed their experimental data by dividing the meausered $pK^+\Lambda$ final state it by simulations that assumed a direct $pK^+\Lambda$ production according to phase space. The peaked distributions observed in the deviation spectra of the MM$_{K^+}$ and IM$_{p\Lambda}$ have been interpreted as a signature of the ppK^- state. A similar study for the HADES data is presented in this subsection.

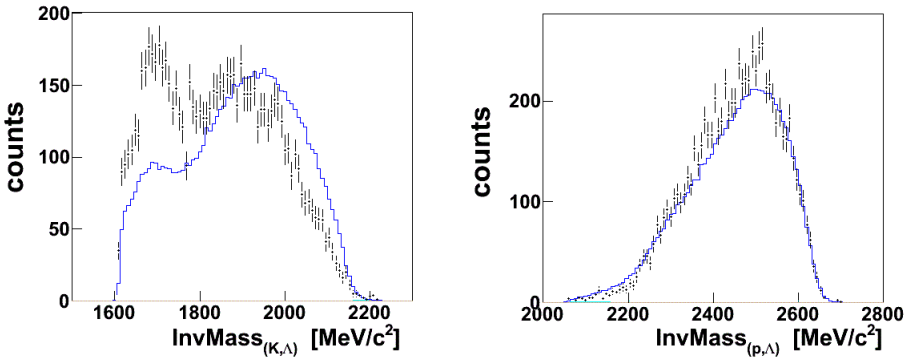

Figure 6.1: Left: IM$_{\Lambda K^+}$ and Right:IM$_{p\Lambda}$. The dots represent the experimental data and the blue line corresponds to the simulation of the $pK^+\Lambda$ channel according to COSY angular distribution (see text for details).

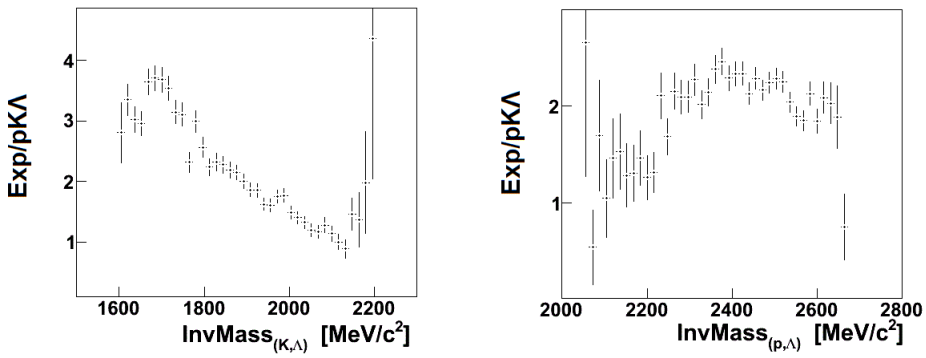

Figure 6.2: Left: $IM_{\Lambda K^+}$ and Right: $IM_{p\Lambda}$ deviation spectra obtained dividing the experimental data by the $pK^+\Lambda$ simulations.

Figure 6.1 shows the $IM_{p\Lambda}$ and $IM_{\Lambda K^+}$ for the HADES experimental data together with the simulated direct $pK^+\Lambda$ production. It is known from other experimental data that the angular distribution of the Λ in the $pK^+\Lambda$ final state is not flat. For our simulations, we have folded the θ_Λ polar angle with the distribution reported in [11] extracted from p+p data at 3200 MeV/c momentum beam energy. The $IM_{\Lambda K^+}$ shows a double peak structure with peaks at 1700 MeV/c^2 and 1900 MeV/c^2 which can not be described by the simulation, whereas the $IM_{p\Lambda}$ can actually be well fitted with the direct $pK^+\Lambda$ production. The deviation spectra for these two observables is shown in fig. 6.2. These deviation spectra were obtained by dividing the experimental data by the simulated direct $pK^+\Lambda$ production. One can see that the deviation spectrum for the $IM_{\Lambda K^+}$ shows a single peak at 1700 MeV/c^2. If the two original peaks seen in this observable were produced by N*-resonances, one could expect to straight forward see two peaks in the deviation spectrum, which is obtained by dividing the experimental data by a phase space distribution. The pΛ invariant mass deviation spectrum shows no visible peaks which means it can be well described by the simulated data.

The Dalitz plots obtained by using these two observables ($IM_{p\Lambda}$ and $IM_{\Lambda K^+}$) are shown in fig. 6.3. The experimental data shows a high contribution of events for high $IM_{p\Lambda}$ and low $IM_{\Lambda K^+}$, whereas the simulated data shows a high number of events for higher $IM_{\Lambda K^+}$ due to the detector's geometry, which is reflected as a diagonal band on the figure. Thus, the deviation spectra has a high number of events for low $IM_{\Lambda K^+}$, meaning that, the direct $pK^+\Lambda$ production can not reproduce correctly these observables from the experimental data.

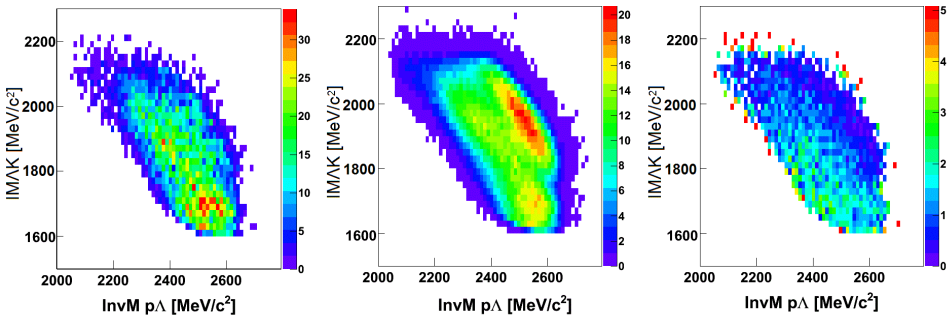

Figure 6.3: Dalitz plot ($IM_{p\Lambda}$ and $IM_{\Lambda K^+}$). Left: experimental data. Middle: Simulated data. Right: Deviation spectrum.

The kinematical properties of the outcoming particles must also be well described by simulation. Figure 6.4 shows the momentum for the Kaon and the outcoming proton in the pp CMS. The kaon momentum for experimental and simulated data are similar and thus, the corresponding deviation spectra shown in fig. 6.5 has no peaks. The momentum of the proton can not be explained using the direct $pK^+\Lambda$ production simulation, as a visible peak for high momentum in the experimental data overcomes the simulated phase space distribution. This is also reflected in the deviation spectra, showing a clear slope for the proton momentum.

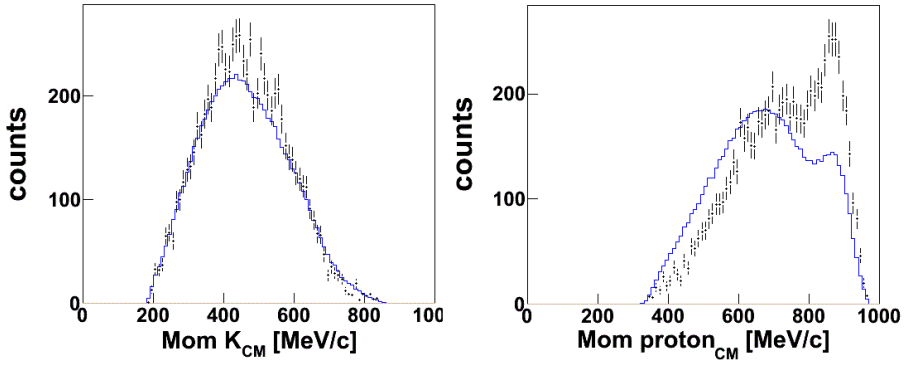

Figure 6.4: Left: Kaon momentum and Right: Proton momentum simulated direct $pK^+\Lambda$ production together with the experimental data.

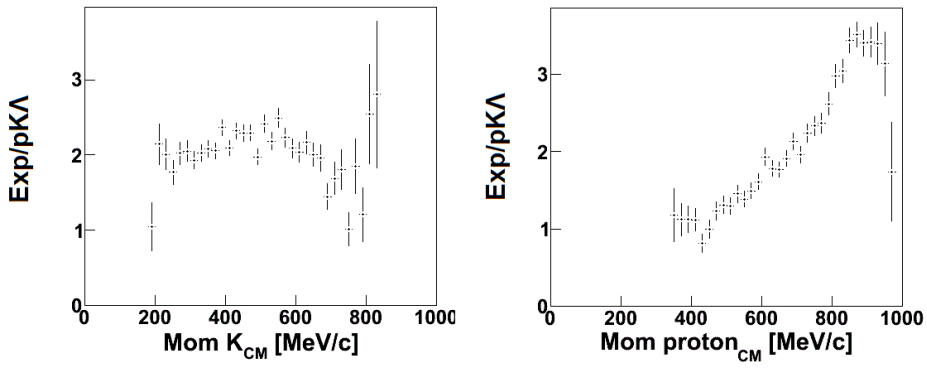

Figure 6.5: Left: Kaon momentum and Right: Proton momentum deviation spectra.

Figure 6.6 shows the angular distribution for both proton and kaon in the pp CMS. The left panel corresponds to the angle for the kaon, which shows a slightly shifted spectra toward low angles for the simulated data. The proton angle (right panel) shows higher number of events for experimental data at low angles. This behavior is also reflected in the deviation spectra shown in fig. 6.7. The kaon shows a broad beak centered at 0 and the proton shows a slope which again means that the direct $pK^+\Lambda$ production does not reproduce the experimental data.

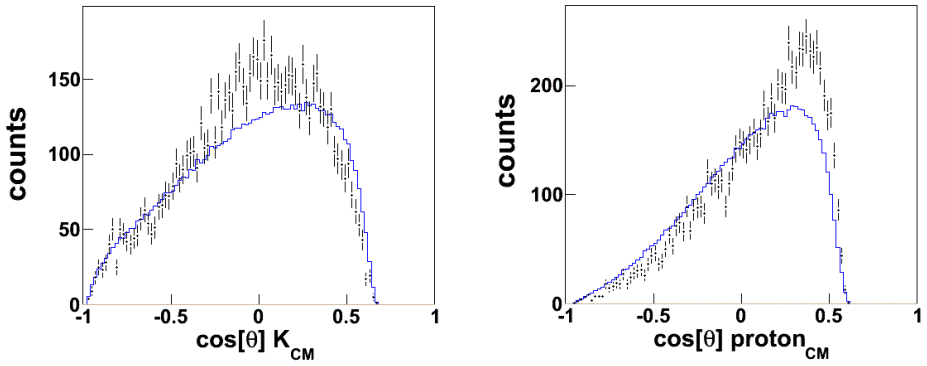

Figure 6.6: Left: Kaon angular distribution and Right: Proton angular distribution simulated direct $pK^+\Lambda$ production together with experimental data.

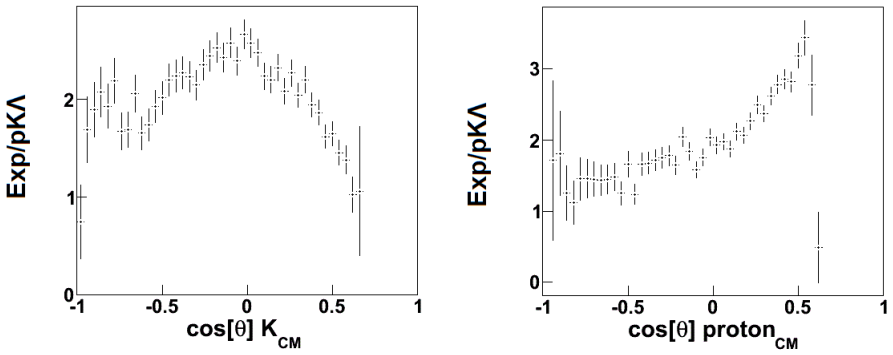

Figure 6.7: Left: Kaon angular distribution and Right: Proton angular distribution deviation spectra.

Finally, the angular distribution between the K^+ and the Λ at the $p\Lambda$ CMS was studied, as a strong angular correlation between the two particles reflects the contribution of an intermediate N*-resonance for the $pK^+\Lambda$ production. Figure 6.8 shows the angular distribution for experimental data and simulated direct $pK^+\Lambda$ production together with the deviation spectra. One can see that the simulation does not reproduce at all the experimental data as the simulated data is shifted toward lower $\cos\theta^{p\Lambda RF}_{K^+\Lambda}$ as compared with simulated data. This behavior is also reflected in the deviation spectrum, producing a straight increasing slope.

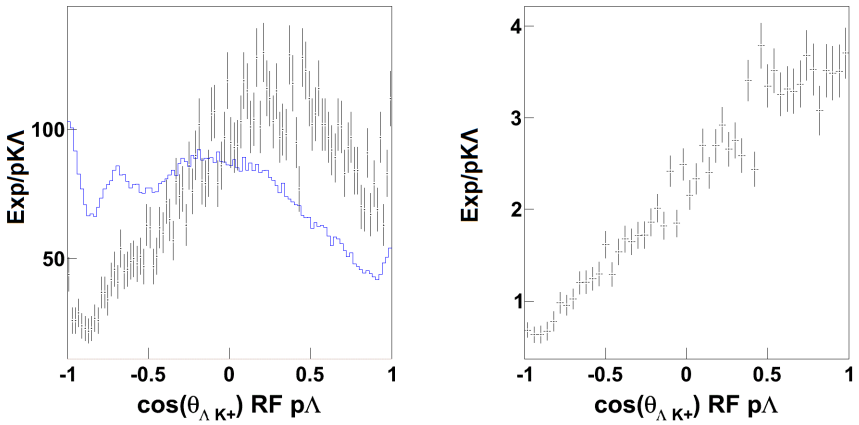

Figure 6.8: $\cos(\theta_{\Lambda K^+})$ at the $p\Lambda$ CMS. Left: simulated and experimental data. Right: Deviation spectrum.

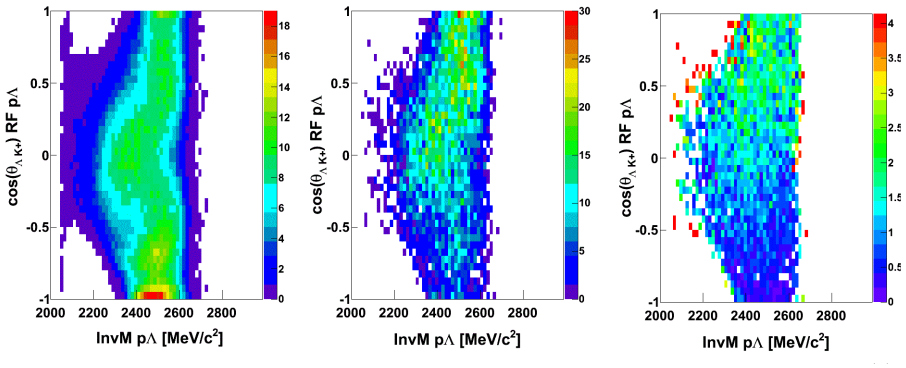

Figure 6.9: $IM_{p\Lambda}$ vs. $\cos(\theta_{\Lambda K^+})$ at the $p\Lambda$ CMS. Left: Simulated data, Middle: Experimental data and Right: Deviation spectrum.

Figure 6.9 shows the $\cos\theta^{p\Lambda RF}_{K^+\Lambda}$ vs. $IM_{p\Lambda}$ for simulated data, experimental data and deviation spectrum which again reflect the totally different shape for the opening angle of the K^+ and the Λ at the $p\Lambda$ CMS for the simulated and the experimental data. The contribution of N*-resonances in the experimental data is then obvious, as a stronger correlation between the K^+ and the Λ than for the direct $pK^+\Lambda$ production is visible.

6.3 Data description by a N* cocktail

As just discussed, the experimental data cannot be described by a direct $pK^+\Lambda$ production, which means that other channels must be introduced in the simulation. Moreover it is well know [17] that a consistent fraction of the total $pK^+\Lambda$ yield stems from intermediate N* resonances. In section 4 and 5 the N*-resonances were studied. The outcoming signal for the studied observables from these resonances depended on their mass, and had a totally different shape to the direct $pK^+\Lambda$ production observables the smaller the N* mass was. Introducing N*-resonances with four different masses in the simulation might help to understand the experimental signal, and whether the simulation of the mixture of these five channels can totally reproduce the experimental data.

An observable to see if the particles in the $pK^+\Lambda$ final state are produced according to phase space or stem from the N^{*+} resonance decay is the invariant mass distribution of $K^+\Lambda$ that is shown in observable is shown in fig. 6.10 c). Figure 6.10 shows four selected mass distributions for the experimental data. The $IM_{K^+\Lambda}$, which should show the mass of the K^+ and Λ mother particle, the MM_{K^+} and $IM_{p\Lambda}$ which should show the mass of a ppK^- state and MM_Λ which also reflects the event kinematics of the $pK^+\Lambda$ production. The $IM_{K^+\Lambda}$ mass distribution shows a clear deviation from a distribution according to a pure phase space. It is described by a two peak structure. One of the peaks is around 1700 MeV/c^2 and the second one at 1900 MeV/c^2.

To obtain a proper description of the experimental data, a cocktail including the direct $pK^+\Lambda$ production and different N* resonances has been employed. The different N* resonances used

here are summarized in table 6.2. From measurements of the COSY-TOF collaboration [11] it is known that none of the three particles in the final state is produced with an isotropic distribution of the polar angle in the CM frame. An angular distribution was included in the simulation of both the N*-resonances and the $pK^+\Lambda$ direct production by weighting the events according to the θ_Λ polar angle for the Λ particle in the center of mass frame with the COSY-TOF measured distribution. The simulated channels were fitted to the experimental distributions. The best fit was determined by a χ^2 minimization of the scaled sum to the measured data. Hereby all distribution in fig. 6.10 were fitted simultaneously. The experimental data could be reproduced assuming a contribution by the N*(1720), N*(1900) and direct $pK^+\Lambda$ production of 41.5%, 57% and 1.5% respectively. The contribution of the $N^*(1650)^+$ and $N^*(2190)^+$ was found to be of 0% for both. A total χ^2 value of 3.18 was obtained.

N* Mass [MeV/c^2]	1650	1720	1900	2190
N* width [MeV/c^2]	165	200	180	500
PDG evidence	***	**		*

Table 6.2: Masses and width used for N*-resonances. Extracted from PDG particle data. [10]

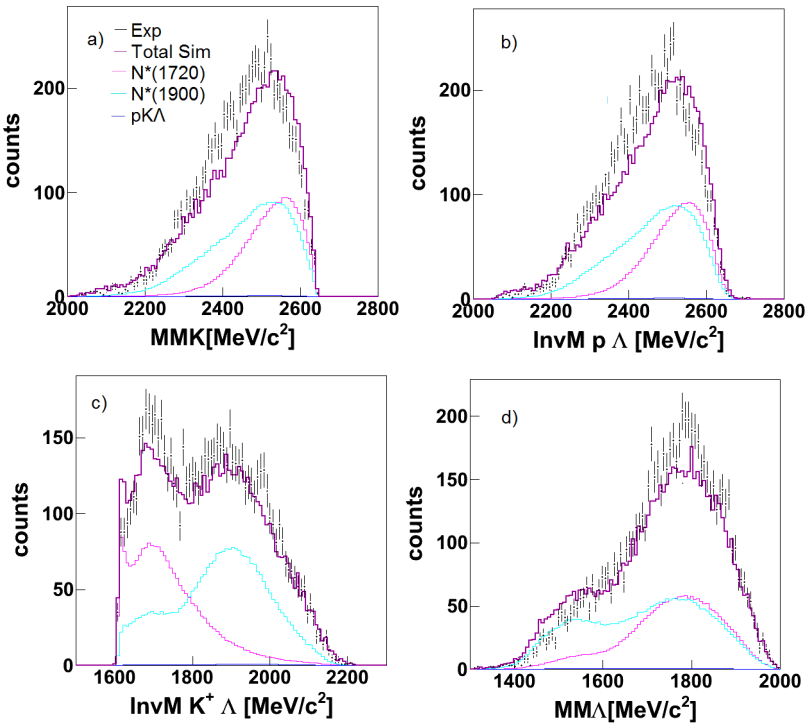

Figure 6.10: a) $IM_{K^+\Lambda}$, b) $IM_{p\Lambda}$,c) MM_{K^+} and d) MM_Λ fitted with the sum of the four N^{*+}-resonances from table 6.2 and the simulation of a direct $pK^+\Lambda$ production.

The result for the fitting is shown in fig. 6.10. One can see the experimental data (black points) for a) $IM_{K^+\Lambda}$, b) $IM_{p\Lambda}$, c) MM_{K^+} and d) MM_{Λ} together with the total sum of the simulated data (purple line) and the contribution from each N* resonance to the final state ((pink) N*(1700), (turquoise) N*(1900), (blue) direct $pK^+\Lambda$ production). As the contribution of the latter is very low compared to the other two channels, it is practically not visible in the figures.

The first panel shows the $IM_{K^+\Lambda}$, which can be well explained with the simulated channels, whereas the next two observables ($IM_{p\Lambda}$ and MM_{K^+}) show that the simulated data is slightly shifted to higher masses compared to experimental data. The last panel shows MM_{Λ}, with an excess of yield compared to the experimental data at low masses around 1500 MeV/c^2 and a lower yield at higher masses around 1800 MeV/c^2.

Figure 6.11 a) shows the simulated Dalitz plot ($IM_{p\Lambda}$-$IM_{K^+\Lambda}$) which was obtained using the mixture of N* and $pK^+\Lambda$ events obtained by the fitting procedure of the one dimensional mass distributions of fig. 6.10. The maximum of the yield is located in a region of the diagram with high $IM_{p\Lambda}$ and low $IM_{K^+\Lambda}$, corresponding to the zone where, at the $K^+\Lambda$ rest frame, the proton has a high momentum and the K^+ and the Λ have a low momentum [1]. This larger yield is caused by the geometrical acceptance of the HADES detector. Figure 6.11 b) corresponds to the same Dalitz plot for the experimental data, which shows a similar distribution like the simulations. Note that the Dalitz plots where not made with the square of each of the observables, following [24].

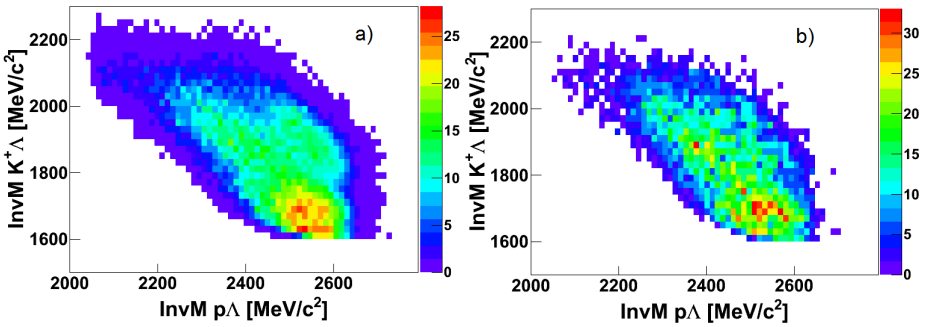

Figure 6.11: Dalitz plot ($IM_{p\Lambda}$-$IM_{K^+\Lambda}$): a) for simulation obtained with the N* and $pK\Lambda$ cocktails (see text for details), b) experimental data.

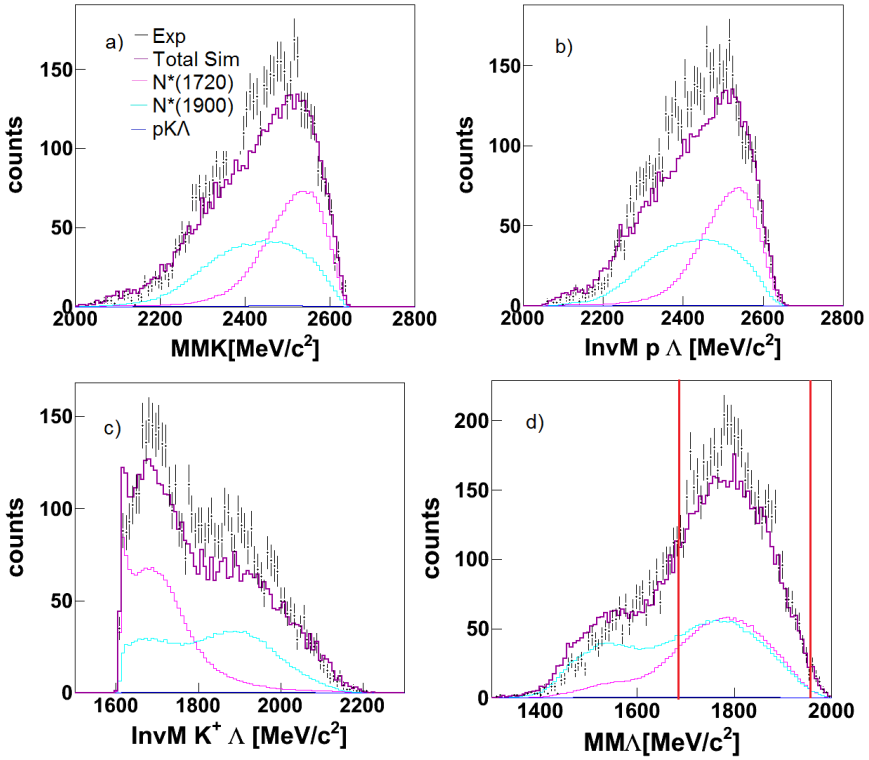

Figure 6.12: a) $IM_{K^+\Lambda}$, b) $IM_{p\Lambda}$, c) MM_{K^+} fitted with the total simulated data (purple line). N*(1700) (pink), N*(1900) (turquoise), direct $pK^+\Lambda$ decay (blue). Cut applied: 1685 MeV/c^2 < MM_Λ < 1950 MeV/c^2.

When studying the simulated data in section 5, it was shown that a cut on the MM_Λ could actually improve the contribution of the ppK^- to the final signal. For fig. 6.12 and 6.13 this cut on the MM_Λ was applied (1685 MeV/c^2 < MM_Λ < 1950 MeV/c^2). In fig. 6.12, the sum of the simulations (purple curve) is slightly lower than the data (black points) for all three observables. The visible peak at 2000 MeV/c^2 in the $IM_{K^+\Lambda}$ (fig. 6.12 a)) is considerably reduced after applying the MM_Λ selection. For the other two observables, $IM_{p\Lambda}$ and MM_{K^+}(a) and b), respectively), the simulation describes the yield at high and low masses but underestimates the yield in the intermediate mass range.

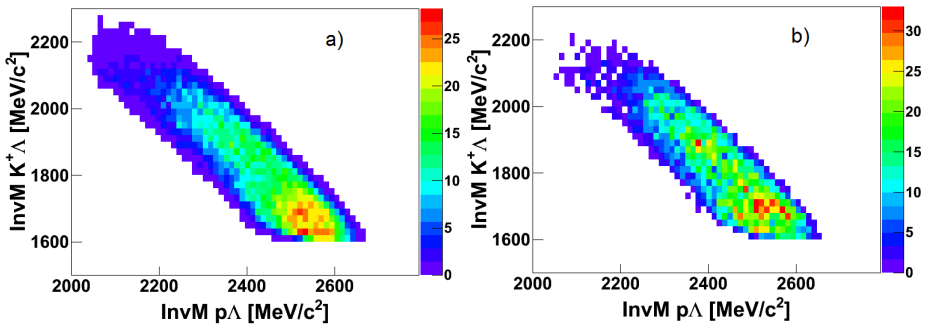

Figure 6.13: Dalitz plot ($IM_{p\Lambda}$-$IM_{K^+\Lambda}$): a) and b) correspond to simulation and experimental data respectively. Cut applied: 1685 MeV/c^2 < MM_Λ < 1950 MeV/c^2.

Figure 6.13 shows the same the Dalitz plot ($IM_{p\Lambda}$-$IM_{K^+\Lambda}$) as fig. 6.11, after that the MM_Λ selection was also applied, following the results of section 5 to improve the ppK^- contribution to the final signal. The left picture corresponds to the simulated spectra. The right picture corresponds to the experimental data. An important influence on the area of the Dalitz plot for both experimental and simulation is noticeable after the selection. This selection on the MM_Λ turns the distribution in the Dalitz plot into a narrow band.

6.4 Momentum and opening angle

In the published results from the DISTO collaboration [22] it was claimed that applying a cut on the proton polar angle at the pp CMS, $\left|\theta_p^{CM}\right|$<0.6 and the kaon polar angle at the pp CMS -0.2<cosθ_{K^+}<0.4 one could reject events which contained the direct $pK^+\Lambda$ production:

$$p + p \rightarrow pK^+\Lambda \tag{6.4.1}$$

A similar analysis based on these observables has been applied to the HADES data, to compare the results.

The simulated data must not only must reproduce the mass observables, but also the kinematics of the outcoming particles. The opening angle of the kaon at the pp CMS gives information of the events which might contain a ppK^- bound state, as large polar angles for the K^+ at the pp CMS might enhance events containing ppK^- bound state [22].

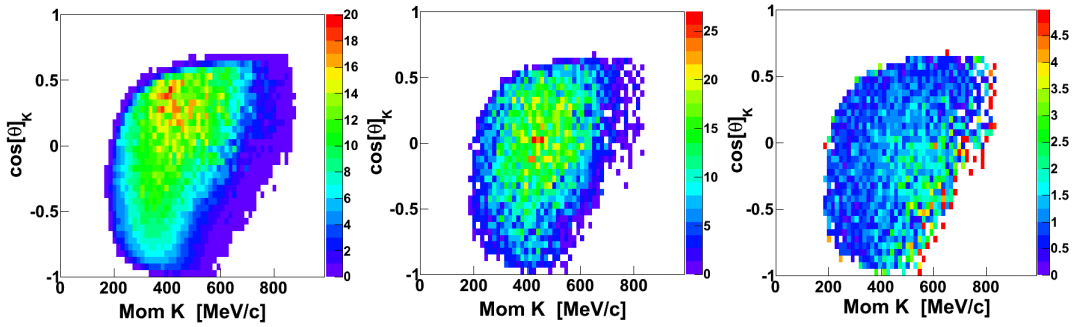

Figure 6.14: cos(θ) - Momentum for simulations (left), experimental data (middle), deviation spectra (right) for the K^+ at the *pp* CMS.

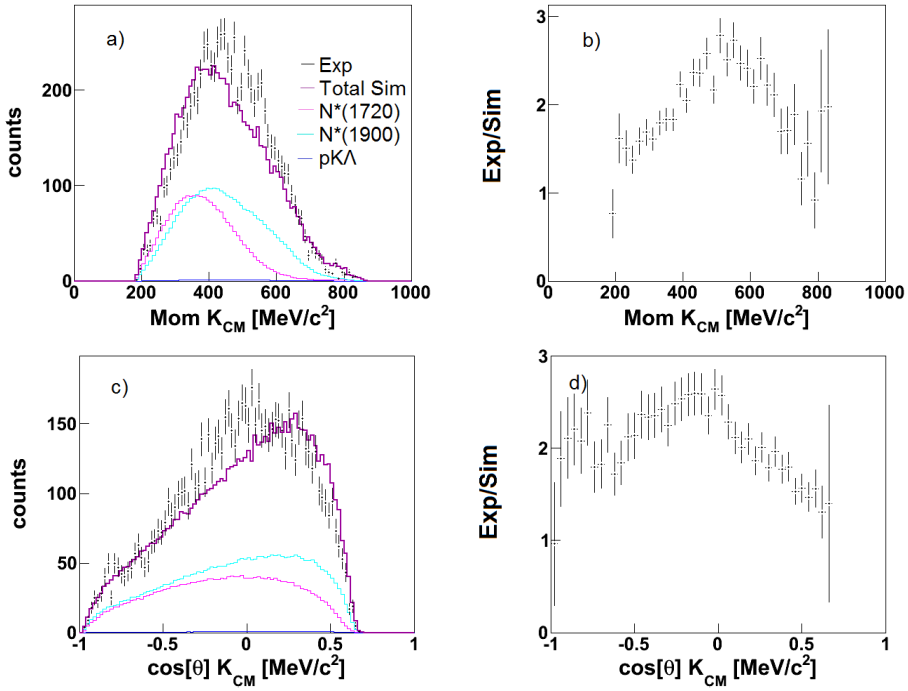

Figure 6.15: Momentum (upper) and cosθ (lower) for simulation and experimental data (left) and deviation spectra (right) for the K^+ at the *pp* CM.

Figure 6.14 shows the cosθ^{CM} vs. momentum for the simulated events, experimental data and the deviation spectra for the K^+ at the pp CMS. The deviation spectra was obtained by dividing the measured distributions by the simulated sum of scaled channels explained previously. Figure 6.15 shows the two projections of the two-dimensional plot shown in fig. 6.14. The projections

for the experimental data and simulation are shown together in panel a) and c). The ratio of the experimental data and simulation is shown in panel b) and d). A high contribution of events with kaon momentum distributed around 500 MeV/c at the pp CMS and large opening angles to the beam axis can be observed. In panel a) and c) of fig. 6.15 a systematic shift between experiment and simulation is visible. The ratio between experiment and simulation in panel b) and d) shows a clear deviation from unity which results in a peak. This means that the simulation does not model the kinematics of the experiment properly.

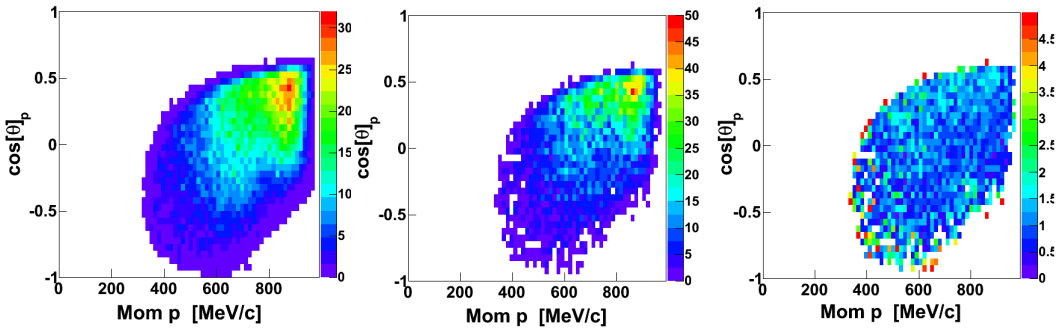

Figure 6.16: Momentum - $\cos\theta^{CM}$ simulated (left), experimental data (middle), deviation spectra (right) for the proton at the pp CM.

Figure 6.16 shows the $\cos\theta^{CM}$ vs. momentum for the simulated, experimental data and deviation spectra for the proton at the pp CMS. The one-dimensional deviation projections for the proton at the pp CMS are shown in fig. 6.17. There are two visible peaks in the proton momentum distribution (fig. 6.17 a))which can be interpreted as the result of the production of the N^{*+} resonances. The primary proton produced together with the light $N^*(1720)^+$ has a larger momentum than a proton produced together with a heavy $N^*(1900)^+$. This two body kinematics in the production process is reflected in a narrow momentum distribution.

The deviation spectrum for the momentum distribution of the proton looks rather flat, which means that the simulation describes the proton kinematics well in first approximation. Figure 6.17 d) is also interesting. Here, the angular distribution deviation spectra is shown. A tendency of larger yield in experiment for forward and backward angles is seen. Notice that only the Λ particle was given a fit function for its angular distribution at the pp CMS. A need to adapt the simulation with angular distribution of the proton in the pp CMS is here obvious.

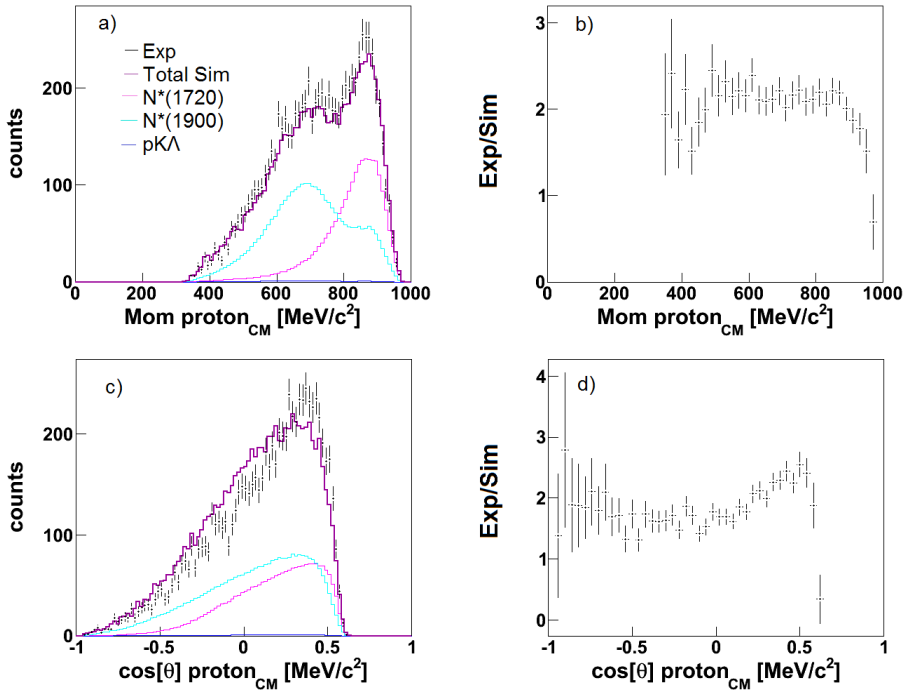

Figure 6.17: a) Momentum and c) cosθ (lower) for simulation and experimental data and deviation spectra b) and d) for the proton at the pp CM.

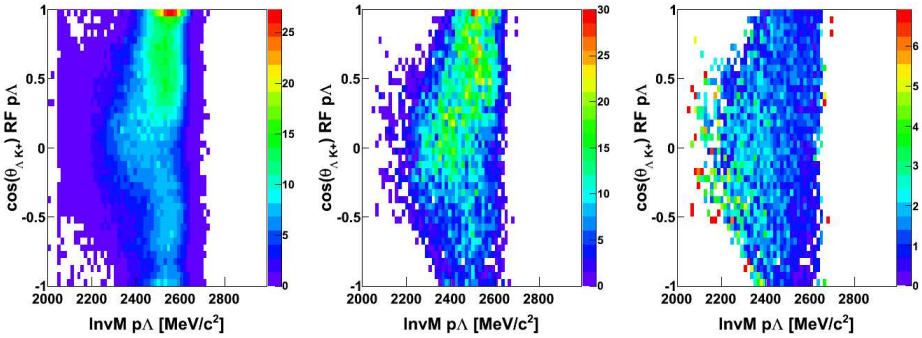

Figure 6.18: IM$_{p\Lambda}$ vs. cos($\theta_{\Lambda K^+}$) at the $p\Lambda$ CMS. Left: Simulated data, Middle: Experimental data and Right: Deviation spectrum.

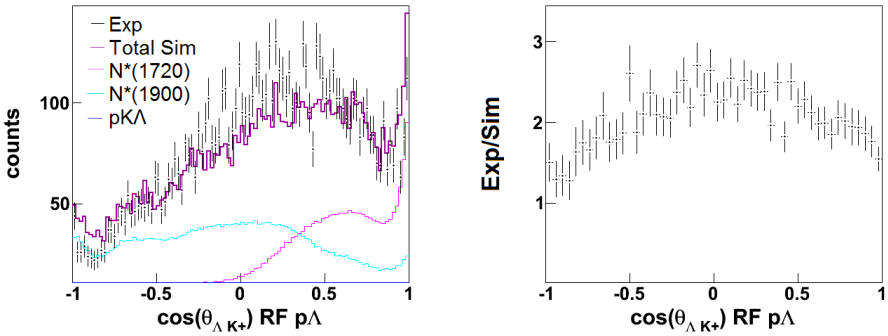

Figure 6.19: $\cos(\theta_{\Lambda K^+})$ at the $p\Lambda$ CMS. Left: simulated and experimental data. Right: Deviation spectrum.

The angular correlation between the K^+ and the Λ at the ppK^- rest frame gives further information about the decay process, as an N* resonance will produce the two particles together with a strong angular correlation, depending on the resonance mass. Figure 6.18 shows the $\mathrm{IM}_{p\Lambda}$ vs. $\cos(\theta_{\Lambda K^+})$ at the ppK^- rest frame (or $p\Lambda$ CMS). The left panel corresponds to the simulated data, which shows a high number of events contributing to small opening angles for the Λ and the K^+ and an invariant mass of approximately 2500 MeV/c^2. The middle panel corresponds to the experimental data and shows a similar behavior as the simulation. This can also be seen through the deviation spectrum (right panel), which shows a relatively flat behavior for the opening angle, and a slightly higher number of events to low $\mathrm{IM}_{p\Lambda}$, meaning that the opening angle can be well reproduced through the simulation, whereas, as will be discused in the next subsection, the $\mathrm{IM}_{p\Lambda}$ can not be correctly reproduced through this first simulation analysis.

Figure 6.19 shows the projected y-axis of fig. 6.18 corresponding to $\cos(\theta_{\Lambda K^+})$ for experimental and simulated data (left panel). The experimental opening angle can be well reproduced by the simulation of the two N^{*+}-resonances. One clearly sees in the simulation, that the opening angle of ΛK^+ coming from the decay of light N^{*+} is smaller as compared to the heavier resonance, as the particles obtain less energy from the resonace's decay. The deviation spectra (right panel) shows a relatively flat behavior. This behavior for the $\cos(\theta_{\Lambda K^+})$ at the $p\Lambda$ CMS shows a highly correlated Λ and K^+ which means that most of the experimental data corresponds to N^{*+}-resonance production.

6.5 Mass Deviation Spectra

As explained at the end of section 5, there are two ways to extract the ppK^- signal from the experimental data. The deviation spectra of the observables which may show a ppK^- signal is studied in this subsection.

Figure 6.20 shows the deviation spectra for the Dalitz plot before (left) and after (right) the MM_Λ cut is applied (1685 MeV/c^2 < MM_Λ < 1950 MeV/c^2). Figure 6.21 shows the deviation spectra (EXP/SIM) for the $IM_{K^+\Lambda}$ and $IM_{p\Lambda}$ distributions before (up) and after (down) applying a cut on the MM_Λ. On the one hand, the $IM_{K^+\Lambda}$ before the cut shows practically a flat shape except for the low mass region which shows an inclined slope until it reaches 1700 MeV/c^2. On the other hand the $IM_{p\Lambda}$ shows a clear deviation from a flat distribution which could lead to two conclusions.

First, one sees a broad peak centered at 2400 MeV/c^2 covering the whole mass range or second, the description of the background is not yet sufficient to draw conclusions from this observable. At this preliminary stage of the analysis the latter explanation is the more promising one. This is also strengthened by the observations in fig. 6.10 a) and b), where a systematic shift of the simulation towards the experimental data was observed. The origin of this peak has to be studied in detail.

It has to be reminded that the angular distribution of the N*-resonant channels as well as the exact mass and width of these intermediate resonances are not yet well known. A further data analysis must be done with an improved analysis for the N*-resonances.

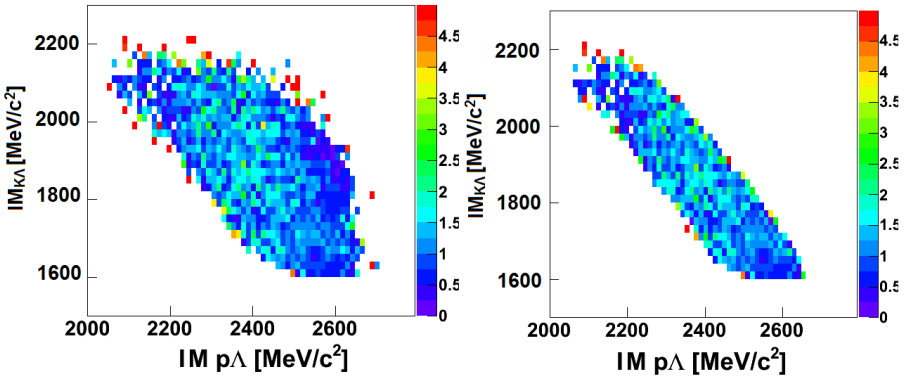

Figure 6.20: Deviation spectra of the Dalitz plot. (Right) cut applied: 1685 MeV/c^2 < MM_Λ < 1950 MeV/c^2.

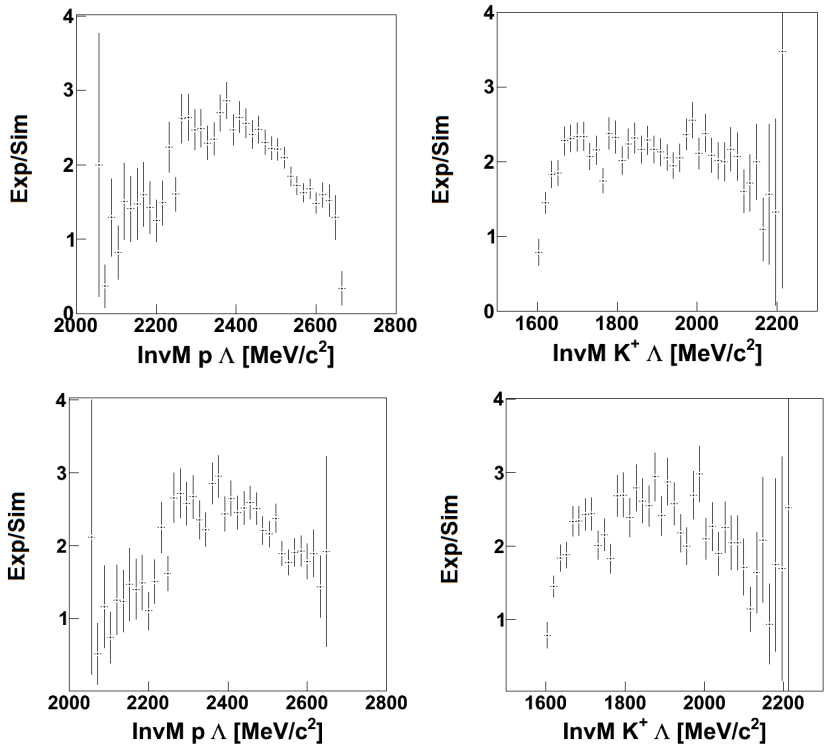

Figure 6.21: $IM_{p\Lambda}$-$IM_{K^+\Lambda}$ deviation spectra before (upper) and after (lower) MM_{Λ} cut.

A similar analysis to the one performed by the DISTO collaboration was considered for this data analysis. They applied a cut on the polar angle of the proton in the pp CMS ($0.6>|cos\theta_{CM,p}|$) with the intention to suppress the direct production of $pK^+\Lambda$. Figure 6.22 shows the $cos\theta_{CM,p}$ vs. momentum of the DISTO experiment. Compared to the distribution in fig. 6.17 it is obvious that this cut does not affect the event selection, in our case, as small polar angles for the proton are not accessible due to the limited geometrical acceptance of the HADES spectrometer.

Finally, the DISTO collaboration showed the $IM^2{}_{p\Lambda}$ vs $\cos\theta_{K^+}$ deviation spectra at the pp CMS [22] for both large and small proton polar angles (fig. 6.23). The deviation spectra obtained by the DISTO collaboration was obtained by dividing the measured distributions by a simulation of direct $pK^+\Lambda$ production according to phase space. The outcoming results showed, for the large proton angle cut, a peak at approximately 5.2 $[GeV/c^2]^2$ and a high number of events for low K^+ polar angle. The $IM^2{}_{p\Lambda}$ vs $\cos\theta_{K^+}$ deviation spectrum for the HADES data is shown in fig. 6.24. A similar result like for the DISTO data can be observed. A large portion of the statistics contribute to events with low polar angle for the K^+, although these events correspond to a higher $IM_{p\Lambda}$ than the one published by DISTO (M=2265 MeV/c^2, Γ=118 MeV/c^2) [22].

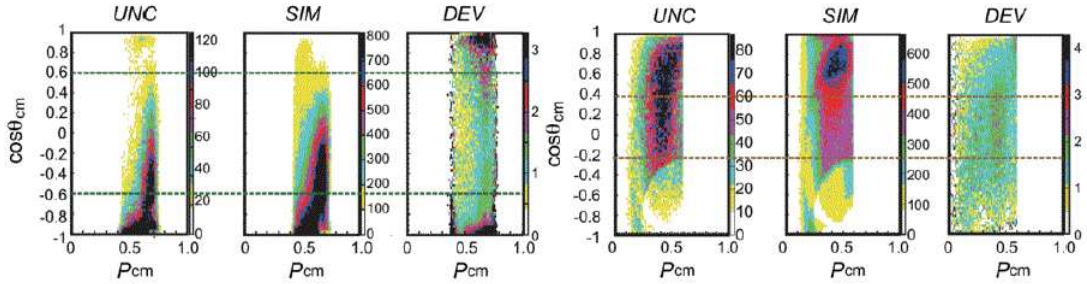

Figure 6.22: Momentum vs. cosθ at the CMS for uncorrected experimental (UNC), Simulated (SIM) and deviation (DEV) spectrum for (left) proton and (right) kaon published on [22]. The dashed lines show the cuts applied on fig. 1.8.

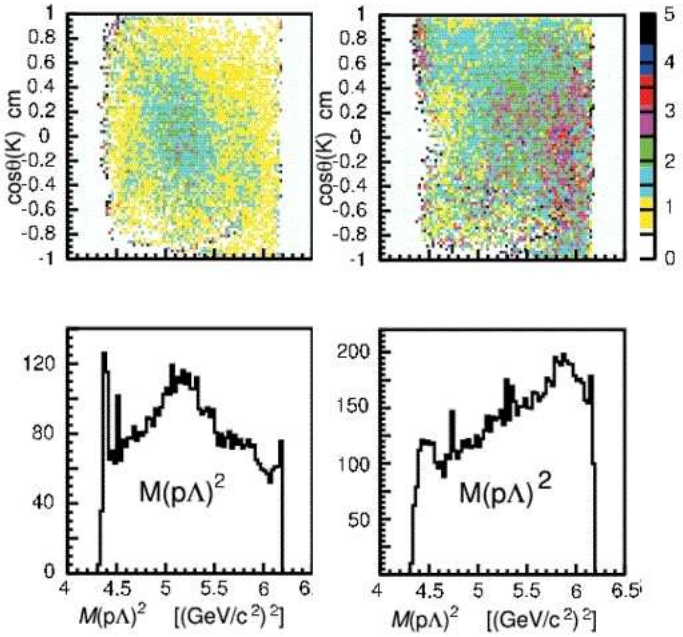

Figure 6.23: DISTO experimental results for the $IM^2_{p\Lambda}$ vs cosθ_{K^+} deviation spectrum. (Left) Large angle proton cut, (right) Small angle proton cut.

A further cut on the kaon polar angle might still reduce the background contribution to the final signal, as the DISTO cut is more restrictive for the kaon than for the proton and the HADES cos$\theta^{CM}_{K^+}$ shows a similar behavior to the DISTO data. Figure 6.25 shows the deviation spectra for the $IM_{p\Lambda}$ after the kaon polar angle cut (-0.2<cosθ_{K^+}<0.4). This shows basically no effect on the ratio.

After a first study on the experimental data measured by the HADES spectrometer, not all observables can be reproduced by simulations. A high contribution of N^{*+} resonances with different masses is visible during all the analysis through the $IM_{K^+\Lambda}$ observable or the $K^+\Lambda$ angular correlation, but still the $IM_{p\Lambda}$ deviation spectra shows a non-flat shape. A further study on the N^{*+} resonances has to be done in order to get a consistent conclusion of the analyzed data.

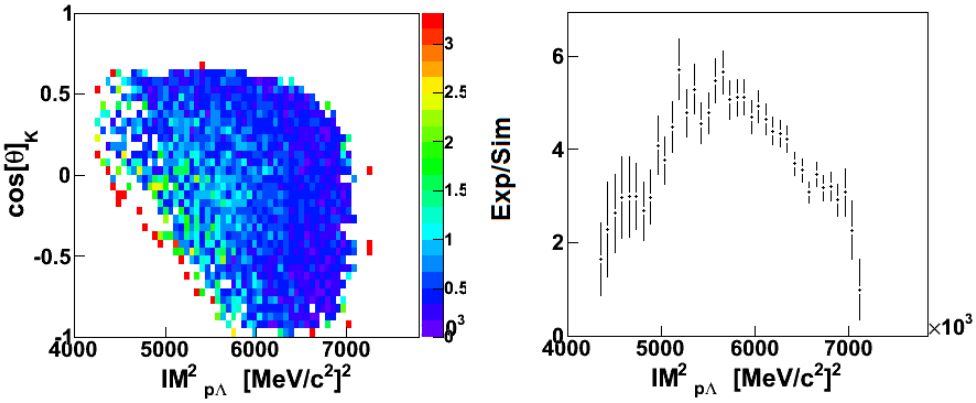

Figure 6.24: $IM^2{}_{p\Lambda}$ vs $\cos\theta^{CM}$ at the pp CM.

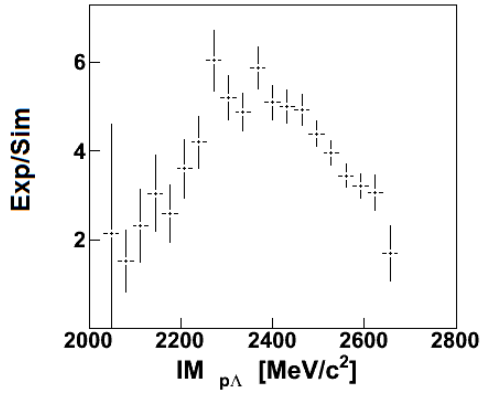

Figure 6.25: $IM_{p\Lambda}$ deviation spectra for -0.2<$\cos\theta_{K^+}$<0.4.

Chapter 7

Conclusions and Outlook

7.1 Conclusions

A strong attractive interaction between a K^- and a proton might lead to a bound state such as the ppK^-. Phenomenological approaches predicted such states and this has triggered the search of these states in several experiments in the last decade. The experiment techniques are very different from one another, ranging from the usage of stopped and in-flight kaons and protons induced reactions. A first analysis using the HADES data of a p+p collision at a kinetic beam energy of 3.5 GeV for the search of the possible existence of the ppK^- was carried out in the framework of this master thesis. The ppK^- bound state was simulated with a mass of 2.332 GeV/c^2 and width 0.06 GeV/c^2. A further study on the ppK^- simulated together with different background simulated channels was done in order to study the feasibility of the measurement of such a state with the HADES spectrometer and develop ad-hoc cuts to improve the signal-to-background ratio. The main background channels used were the direct production of a $pK^+\Lambda$ final state and through the decay of intermediate N*-resonances. We have shown that under the made assumptions the measurement of the ppK^- state is feasible using HADES and the collected data set for the p+p at 3.5 GeV reaction.

A further study using the experimental data was done following the DISTO experimental analysis of the DISTO collaboration [22]. First, the IM$_{p\Lambda}$, IM$_{\Lambda K^+}$ and the proton and kaon kinematics were tried to be described by a direct $pK^+\Lambda$ production using the COSY-TOF angular distribution for the Λ particle [11]. This first fit using a direct $pK^+\Lambda$ production simulation was done which did not properly explain the measured data. A second fit using four different intermediate N* resonance masses and the direct $pK^+\Lambda$ production was done. This last fit could reproduce better both the observables and the outcoming particles kinematics, although the IM$_{p\Lambda}$ and the angular distribution for the outcoming proton at the pp CMS still showed some structures in the deviation spectra.

In general, we have shown that in order to extract the contribution of possible exotic states from p+p collisions in the $pK^+\Lambda$ final state, a quantitative knowledge of the non-exotic channels is necessary.

7.2 Outlook

A more precise study of the simulation in order to reproduce not only the mass but also the kinematics of the outcoming particles should be done. As explained when analyzing the experimental data, the angular distribution for the N*-resonances are not yet well known, and thus a further analysis has to be carried out. A more complete method would be to employ partial wave analysis to interpret the extracted $pK^+\Lambda$ signal.

The ppK^- bound state has, not only the $p\Lambda$ decay process, but also a $\Sigma^0 p$ final state, which should be also included in the analysis to obtain more accurate results for the experimental data. Further kinematic cuts may be applied in order to improve the possible ppK^- signal in the experimental data.

Bibliography

[1] E. Byckling, K. Kajantie, *Particle Kinematics, 1973.*

[2] E. Epple, *The Λ(1405)-Resonance measured via its decay into $\Sigma^0\pi^0$ in proton proton collisions with the HADES spectrometer, Diplomarbeit, 2009.*

[3] G. Agakishiev et al. (HADES coll.) *DOI: 10.1007/s 10751 012 056 8*

[4] G. Bendiscioli, et al., *Nuclear Physics A 789 222–242, 2007*

[5] HADES-wiki, *http://hades-wiki.gsi.de/cgi-bin/view*

[6] HADES, *http://www-hades.gsi.de/docs/mdc/mdcana/mdc-essentials.htm*

[7] I. Fröhlich et al. *arXiv:nucl-ex/0905.2568, 2009.*

[8] J. Siebenson, *Exclusive analysis of the Λ(1405) resonance in the charged $\Sigma\pi$ decay channels in proton proton reactions with HADES, Diplomarbeit, 2010*

[9] K. Lapidus, et al., *arXiv: 0904.1128v1 [nucl-ex], 2009*

[10] K. Nakamura et al., Particle Data Group. *Particle Physics Booklet, 2008.*

[11] M. Abdel-Bary, et al., The COSY-TOF collaboration, *arXiv:1008.4287v1 [nucl-ex], 2011*

[12] M. Agnello, G. Beer et al. Phys Rev Lett. 94(21), *2005*

[13] M. H. Alston et al., *Phys. Rev. Lett., 6:698–702, 1961.*

[14] M. Traxler, *Real-Time Dilepton Selection for the HADES Spectrometer, 2001.*

[15] R. H. Dalitz, S. F. Tuan, *Phys. Rev. Lett. 2 425, 1959* .

[16] R. J. Hemingway, et al., *Nucl.Phys. B253 742, 1985*

[17] S. Abd El-Samad, et al., COSY-TOF Collaboration, *arXiv:1003.0603v2 [nucl-ex], 2010*

[18] S. Agostinelli et al. *Nuclear Instruments and Methods in Physics Research A 506 250-303, 2003*

[19] T. Hyodo, W. Weise*, arXiv:0712.1613v3 [nucl-th], 2008*

[20] T. Hyodo, D. Jido, *arXiv:1104.4474v3 [nucl-th], 2011*

[21] T. Yamazaki, Y.Akaishi, *arXiv:0709.0630v2 [nucl-th], 2007*

[22] T. Yamazaki, M. Maggiora, et al., *arXiv:1002.3526v1 [nucl-ex], 2010*

[23] T. Yamazaki, Y. Akahishi, *Phys. Rev. C. 76 045201,2007*

[24] T. Yamazaki, P. Kienle, *Private comunication, 2011.*

[25] T. Yamazaki, Y. Akaishi, *arXiv:nucl-th/0604049v1, 2006*

[26] V. K. Magas, E. Oset, A. Ramos, *Phys.Rev. C 74 2, 2006*

[27] Y. Akaishi et al., *arXiv:1002.2560v1 [nucl-th], 2010*